

Physical Properties of Dense Cores in the ρ Ophiuchi Main Cloud and A Significant Role of External Pressures in Clustered Star Formation

Hajime Maruta¹, Fumitaka Nakamura^{2,3}, Ryoichi Nishi¹, Norio Ikeda³, Yoshimi Kitamura³

ABSTRACT

Using the archive data of the H^{13}CO^+ ($J = 1 - 0$) line emission taken with the Nobeyama 45 m radio telescope with a spatial resolution of $\sim 0.01\text{pc}$, we have identified 68 dense cores in the central dense region of the ρ Ophiuchi main cloud. The H^{13}CO^+ data also indicates that the fractional abundance of H^{13}CO^+ relative to H_2 is roughly inversely proportional to the square root of the H_2 column density with a mean of 1.72×10^{-11} . The mean radius, FWHM line width, and LTE mass of the identified cores are estimated to be $0.045 \pm 0.011\text{ pc}$, $0.49 \pm 0.14\text{ km s}^{-1}$, and $3.4 \pm 3.6 M_{\odot}$, respectively. The majority of the identified cores have subsonic internal motions. The virial ratio, the ratio of the virial mass to the LTE mass, tends to decrease with increasing the LTE mass and about 60 percent of the cores have virial ratios smaller than 2, indicating that these cores are not transient structures but self-gravitating. The detailed virial analysis suggests that the surface pressure often dominates over the self-gravity and thus plays a crucial role in regulating core formation and evolution. By comparing the ρ Oph cores with those in the Orion A molecular cloud observed with the same telescope, we found that the statistical properties of the core physical quantities are similar between the two clouds if the effect of the different spatial resolutions is corrected. The line widths of the ρ Oph cores appear to be nearly independent of the core radii over the range of $0.01 - 0.1\text{ pc}$ and deviate upwards from the Heyer & Brunt relation. This may be evidence that turbulent motions are driven by protostellar outflows in the cluster environment.

Subject headings: ISM: clouds — ISM: individual (ρ Ophiuchi) — ISM: structure — stars: formation — turbulence

1. Introduction

Observations of young stellar populations in the Galaxy have revealed that the majority of stars form in clusters (Lada & Lada 2003; Allen et al. 2006). For example, Lada et al. (1991) performed

¹Department of Physics, Niigata University, 8050 Ikarashi-2, Niigata 950-2181, Japan

²Astrophysics Lab., Faculty of Education, Niigata University, 8050 Ikarashi-2, Niigata 950-2181, Japan

³Institute of Space and Astronautical Science, Japan Aerospace Exploration Agency, 3-1-1 Yoshinodai, Sagami-hara, Kanagawa 229-8510, Japan

an extensive near-infrared imaging survey of the central regions of L1630 in Orion B and found that about 60 – 90 % of all the young stellar populations associated with the molecular cloud form only in three rich embedded clusters. Using the 2MASS point source catalog, Carpenter (2000) estimated the fraction of young stellar populations contained in clusters to be 50 – 100 % for nearby cluster forming molecular clouds such as Perseus, Orion A, Orion B, and MonR2. Recent near-infrared surveys of young stellar populations using the Spitzer Space Telescope have confirmed that clustered star formation is the dominant mode of star formation in the Galaxy (Allen et al. 2006; Poulton et al. 2008; Román-Zúniga et al. 2008). However, previous studies of star formation have focused on star formation in relative isolation, for which the environmental effects that play a crucial role in clustered star formation are thought to be minor or at least secondary. Thus, how stars form in the cluster environment remains only poorly understood.

An important clue to understanding star formation in clusters has come from recent millimeter and submillimeter observations of the nearby cluster-forming region, the ρ Ophiuchi molecular cloud (L1688), which uncovered dense cores with a mass spectrum that resembles the Salpeter IMF (Motte et al. 1998; Johnstone et al. 2000a; Stanke et al. 2006). Similar studies in other star forming regions have confirmed that such a resemblance between the core mass spectrum and the stellar IMF seems to be common in nearby star forming regions (Testi & Sargent 1998; Motte et al. 2001; Reid & Wilson 2006; Ikeda et al. 2007, 2009). These observations suggest that the stellar IMF may be determined to a large extent by the core mass distribution (e.g., André et al. 2007), although mass accretion from ambient gas onto forming stars may sometimes plays an important role in determining the final masses of stars (Bonnell et al. 2001; Bate et al. 2003; Wang et al. 2009). Therefore, it is important to investigate the formation and evolution of dense cores in the cluster environment.

Recent theoretical studies on core formation in the cluster environment have emphasized the role of supersonic turbulence (Klessen et al. 1998; Tilley & Pudritz 2004; Vázquez-Semadeni et al. 2005; Dib et al. 2007). These studies have demonstrated that dense cores are formed in regions compressed by converging turbulent flows. However, the origin of this supersonic turbulence and its role in core formation are still a matter of debate. Two main scenarios have been proposed. In the first scenario, formation of dense cores (and thus star formation) is considered to be completed only in one turbulent crossing time, i.e., one dynamical time, so that the cluster forming regions are destroyed within one dynamical time (Elmegreen 2000; Hartmann 2001; Heitsch et al. 2008). In this case, the mass spectrum of dense cores is shaped by the cascade of primordial interstellar turbulence that has a power law form (Padoan & Nordlund 2002). On the other hand, in the second scenario, star formation is considered to continue at least over several dynamical times. In this case, additional turbulent motions must be replenished to keep supersonic turbulence in molecular clouds because supersonic turbulence dissipates quickly in one dynamical time (Stone et al. 1998; Mac Low 1999). In such circumstances, dense cores are continuously created (and destroyed) in molecular gas disturbed strongly by the additional turbulent motions. In the cluster environment, stellar feedback such as stellar winds, HII regions, and protostellar outflows has been discussed as the dominant

source of additional supersonic turbulence (Norman & Silk 1980; Matzner 2007; Li & Nakamura 2006). Other sources of turbulence such as supernova blastwaves, external cloud shearing, or converging flows of cloud formation may also play a role (e.g., McKee & Ostriker 2007). As for the protostellar outflow-driven turbulence, Swift & Welch (2008) identified the characteristic energy injection scale at ≈ 0.05 pc for the L1551 star forming region where a group of stars are forming, indicating that the protostellar outflows are the primary source of regenerating turbulence in this region. Recently, Offner et al. (2008) performed three-dimensional (3D) hydrodynamic simulations of turbulent molecular clouds and suggested that the physical properties of dense cores may be affected directly by the presence or absence of turbulent feedback, although further justification may be needed. Therefore, to shed light on the issue of core formation in the cluster environment, it is essential to investigate the kinematics of dense cores. In this paper, we thus analyze the physical properties of dense cores in the nearest cluster forming region, the ρ Ophiuchi molecular cloud.

The ρ Ophiuchi molecular cloud is the nearest cluster forming regions at a distance of ~ 125 pc (e.g., Lombardi et al. 2008; Loinard et al. 2008; Wilking et al. 2008). The dense part of the ρ Ophiuchi molecular cloud (hereafter the ρ Ophiuchi main cloud) is known to harbor a rich cluster of young stellar objects (YSOs) in different evolutionary stages (Wilking et al. 2008; Enoch et al. 2008; Jørgensen et al. 2008). Recent millimeter and submillimeter dust continuum observations of the ρ Ophiuchi main cloud have revealed that a large number of dense cores are concentrated in the central dense part of the cloud and their mass spectra are similar in shape to the stellar IMF (Motte et al. 1998; Johnstone et al. 2000a). By comparing with isothermal, pressure-confined, self-gravitating Bonnor-Ebert spheres, Johnstone et al. (2000a) argued that the dense cores detected by the dust continuum emission are likely to be self-gravitating and expected to form stars (see also Johnstone et al. 2004). However, to accurately assess the dynamical states of the dense cores, it is necessary to perform molecular line observations using high density tracers such as H^{13}CO^+ ($J = 1 - 0$) and N_2H^+ ($J = 1 - 0$), both of which have the critical densities for excitation as high as 10^5 cm^{-3} . Recently, the Nobeyama observatory has released the archive data of the H^{13}CO^+ ($J = 1 - 0$) line emission toward the ρ Ophiuchi main cloud taken with the 45 m radio telescope. At a distance of 125 pc, the spatial resolution of the data of $21''$, corresponding to ~ 0.01 pc, is comparable to those of the dust continuum observations, e.g., the SCUBA at the JCMT with a beam size $14''$ at $850 \mu\text{m}$. Thus, the Nobeyama archive data is suitable for analyzing the dynamics of small scale structures comparable to the ones detected by the dust continuum observations. Our analysis is complementary to that of André et al. (2007) who observed several subclumps (Oph A, B1, B2, C, E, and F) with the IRAM 30 m radio telescope using N_2H^+ ($J = 1 - 0$) line to measure the line widths of the dust cores detected by Motte et al. (1998). The H^{13}CO^+ data of the Nobeyama 45 m telescope was taken in a larger area covering the whole dense region of the ρ Ophiuchi main cloud, including all the subclumps observed by André et al. (2007). Since the dense gas detected by molecular line emissions such as H^{13}CO^+ ($J = 1 - 0$) and N_2H^+ ($J = 1 - 0$) may not be always well associated with the dust cores and therefore the line widths of the dust cores estimated by André et al. (2007) may not be accurate, we identified the dense cores directly from the molecular line data cube and estimated their physical quantities such as the core radius, mass,

and line width.

The rest of the paper is organized as follows. First, the description of the archive data is presented in §2. In §3 we show the spatial distribution of the dense gas detected by the H^{13}CO^+ emission, which indicates very clumpy structures. Then, in §4 we identify the clumpy structures as dense cores applying a clump-finding algorithm, the so-called clumpfind (Williams et al. 1994), and derive the physical properties of the identified cores. To accurately evaluate the core masses, the fractional abundances of H^{13}CO^+ relative to H_2 are derived directly by comparing the H^{13}CO^+ column densities with the H_2 column densities obtained from the $850\ \mu\text{m}$ dust continuum emission. In §5 we discuss the mass spectrum of the identified cores and their dynamical states. We also compare the physical properties of the identified cores with those in Orion A, taking into account the effect of different distances (or different spatial resolutions). Finally, we summarize our main conclusion in §6.

2. Data

We used the archive data of the ρ Ophiuchi main cloud taken in H^{13}CO^+ ($J = 1 - 0$) molecular line (86.75433 GHz) with the Nobeyama 45 m radio telescope. The fits data is available from the web page of the Nobeyama Radio Observatory at the National Astronomical Observatory of Japan (<http://www.nro.nao.ac.jp/>). The observations were carried out in the period from 2002 March to 2003 May. All spectra were obtained in the position-switching mode. The data has $118 \times 98 \times 60$ grid points in the α - δ - v_{LSR} space, covering the whole dense region of the ρ Ophiuchi main cloud with size of about $1.5\ \text{pc} \times 1.3\ \text{pc}$. The grid size of the data was $21''$, corresponding to $0.013\ \text{pc}$ at a distance of $125\ \text{pc}$. The main beam efficiency of the telescope was 0.51. We note that the FWHM beam size of the telescope was $18''$ at 87 GHz, and therefore the data were almost full-beam sampled, considering the typical pointing error of a few arcsecond (see the web page of the Nobeyama Radio Observatory). The velocity resolution is $0.13\ \text{km s}^{-1}$ and the average Root Mean Square (rms) noise determined from signal-free channels is $\sigma = 0.11\ \text{K}$ in T_A^* .

3. Distribution of Dense Molecular Gas in the ρ Ophiuchi molecular cloud

3.1. Overall Distribution of the H^{13}CO^+ emission

Here, we present the overall distribution of dense gas observed by the H^{13}CO^+ ($J = 1 - 0$) emission. Figure 1a shows a total integrated intensity map of the H^{13}CO^+ emission toward the ρ Ophiuchi main cloud. For comparison, the $850\ \mu\text{m}$ image obtained with the SCUBA at the JCMT is shown in Figure 1b. While the distribution of the H^{13}CO^+ emission appears to cover a larger area than that of the $850\ \mu\text{m}$ emission, the overall spatial distribution of the H^{13}CO^+ emission is similar to that of the $850\ \mu\text{m}$ emission. We note that it is very difficult to observe extended

structures with bolometers mounted on ground-based telescope due to the atmospheric emission. The extended structures larger than $\sim 1.5'$ (≈ 0.06 pc) are therefore suppressed in removing the atmospheric emission during the data reduction process, making the $850 \mu\text{m}$ map mostly devoid of extended emission (Johnstone et al. 2000b). Our H^{13}CO^+ map shows that the well-known dense subclumps (Oph A, B1, B2, C, E, and F. Note that the Oph D region is out of our area.), previously identified by DCO^+ and other observations, are very clumpy as recent submillimeter observations have revealed (Motte et al. 1998; Johnstone et al. 2000a). In the next section, we identify the clumpy structures as dense cores applying a clump-finding algorithm, clumpfind (Williams et al. 1994), and derive physical properties of the identified cores.

3.2. Individual Regions

Blow-up total integrated intensity maps toward the Oph A and Oph B1, B2 and C regions are shown in Figures 2a and 2b, respectively. Iso antenna temperature surfaces of the same areas in the 3D data space (α - δ - v_{LSR}) are also shown in Figure 3. Our intensity maps can be compared with Figure 2 of André et al. (2007), the N_2H^+ ($J = 1 - 0$) intensity maps obtained with the IRAM 30 m telescope. The beam sizes for both the telescopes are comparable: the HPBW of the IRAM 30 m, $26.4''$, is about 1.5 times as large as that of the Nobeyama 45 m telescope, $18''$. Both the molecules are also expected to trace dense molecular gas in nearly the same density range because the critical densities for excitation of H^{13}CO^+ ($J = 1 - 0$) and N_2H^+ ($J = 1 - 0$) lines are comparable ($n_{\text{cr},\text{H}^{13}\text{CO}^+} = 8 \times 10^4 \text{ cm}^{-3}$ and $n_{\text{cr},\text{N}_2\text{H}^+} = 2 \times 10^5 \text{ cm}^{-3}$). In fact, the distribution of the H^{13}CO^+ emission is remarkably similar to that of the N_2H^+ emission.

The most intense line emission of H^{13}CO^+ ($J = 1 - 0$) comes from the Oph A region. The maximum antenna temperature reaches $T_A^* \simeq 4$ K at the position that coincides with that of a starless object, SM1, identified by André et al. (1993) within our spatial resolution. A prominent feature of this region is a dense ridge running from north to south, which is also seen in the $850 \mu\text{m}$ map. The starless objects SM1, SM1N, and SM2 identified by André et al. (1993) are located just at the densest part of the ridge. Although relatively strong H^{13}CO^+ emission is detected toward VLA1623, the prototypical Class 0 object, it is difficult to distinguish the H^{13}CO^+ emission associated with VLA 1623 from the ambient component because of our resolution as large as $21''$.

In the $850 \mu\text{m}$ map, Wilson et al. (1999) found two filaments in the Oph A region [see Figure 1 of Wilson et al. (1999)]. Similar structures can be recognized in our H^{13}CO^+ map. In the $850 \mu\text{m}$ map, the two filaments (the dashed lines in Figure 2a) intersect at the position (RA, Dec) = ($16^{\text{h}}26^{\text{m}}29^{\text{s}}$, $-24^{\circ}22'45''$; J2000). In the H^{13}CO^+ map, the north-east filament is not seen, whereas the north-west filament, a part of the Oph A ridge, has strong H^{13}CO^+ emission. Such a feature is consistent with that of the N_2H^+ map by Di Francesco et al. (2004), indicating that the north-east filament presumably consist of diffuse warm gas. The filament is reminiscent of the Orion bar where the dust continuum emission enhanced by heating from PDRs and young stars is prominent but the H^{13}CO^+ line emission is not seen (Ikeda et al. 2007). In fact, the location of the north-east

filament agrees well with the edge of the PDR seen in ISO images (Abergel et al. 1996).

In the western side of the Oph A ridge, Wilson et al. (1999) found another interesting structure: two arcs that are labeled with No. 1 and 2 in Figures 2a and 3a. In addition to these two, we identified 3 new arcs in the Oph A region (labeled with No. 3 through 5). Although the No. 1 arc is not clearly recognized as an arc in the total intensity map of Figure 2a owing to the presence of the extended diffuse component, the No. 1 arc as well as the No. 2 and 3 can be clearly seen in the iso-temperature surfaces in Figure 3a. These arcs may be created by the stellar wind from the young B3 star S1. Another possibility is the effect of three outflows detected in this region whose outflow axes are almost parallel in the α - δ space and inclination angles are around 60 – 80 degrees (Kamazaki et al. 2003). One of the three outflows is the most spectacular outflow from the Class 0 object VLA 1623. Both sides of the No. 1 arc extended from VLA 1623, where no H^{13}CO^+ emission is detected, appear to be parts of a cavity created by the VLA 1623 outflow. On the other hand, in the eastern side of the Oph A ridge, we can recognize two new arcs. These arcs (labeled with No. 4 and 5) appear to be related to a giant protostellar outflow that has been recently discovered by Nakamura et al. (2009, in preparation) on the basis of the ^{12}CO ($J = 3 - 2$) observations.

A couple of features that are likely to be created by protostellar outflows are also seen in the Oph B2 region, the densest region after the Oph A. The H^{13}CO^+ map shows a very clumpy structure with ~ 10 local peaks in the region. Many dust cores identified by Motte et al. (1998) are distributed mainly in the bright area of the H^{13}CO^+ map, where some cores identified by the clumpfind in the data cube (see §4) are overlapped on the plane of the sky. It is difficult to distinguish such an overlapped core from the other in the H^{13}CO^+ total integrated intensity map or the dust continuum map that does not have velocity information. In the southern part of the Oph B2 region (labeled with No. 1), a hole is seen in both the H^{13}CO^+ and 850 μm maps. The hole is particularly clear in the data cube in Figure 3b. Two other holes are also seen near the northern (No. 2) and southern (No. 3) edges of the B2 region. These holes are likely to be created by the giant protostellar outflow recently found by Nakamura et al. (2009). The blue lobe of this outflow is extended beyond the B2 region, reaching the No. 4 and 5 arcs. The apparent luminosity and the total mass of this outflow are largest in ρ Oph. The driving source is likely to be a class I YSO Elias 32 or 33. No. 1 and 2 holes are likely to be created by the red and blue lobes, respectively. The interaction between the protostellar outflows and the dense gas will be discussed elsewhere (Nakamura et al. 2009, in preparation). Cavities that could be created by protostellar outflows are also found in NGC1333, a nearby cluster forming clump in the Perseus molecular cloud (Knee & Sandell 2000; Sandell & Knee 2000; Quillen et al. 2005), suggesting that density structures in cluster forming regions are strongly affected by protostellar outflows. Nakamura et al. (2009) also found other examples of the dynamical interaction between the dense gas and the outflows in ρ Oph, which will be shown elsewhere.

4. Physical Properties of Dense Cores

We identified 68 H^{13}CO^+ cores in the ρ Ophiuchi main cloud, using the clumpfind method described in §4.1. Here, we describe physical properties of the identified cores. The definitions of the physical quantities of the cores are presented in §4.2. The fractional abundance of H^{13}CO^+ relative to H_2 , which is important to the determination of core mass, is estimated in §4.3. In §4.4, we describe the statistical properties of the physical quantities of the identified cores, and compare their positions with those of YSOs identified by the Spitzer Space Telescope mid-infrared data (Jørgensen et al. 2008). We also compare our cores with 850 μm cores listed in Table 7 of Jørgensen et al. (2008). Finally, we show in §4.6 the correlation among physical quantities such as the line width-radius and virial ratio-mass relations.

4.1. Core Identification

To identify dense cores from the H^{13}CO^+ data cube, we applied the clumpfind method described in §3.2 of Ikeda et al. (2007). In brief, we adopted the threshold ($T_{A,\text{th}}$) and stepsize (ΔT_A) of the 2σ noise level for core identification, following Williams et al. (1994) who recommended using this set of the parameters based on the results of their test simulations. To identify the cores with reasonable accuracy, we imposed the following 3 criteria: (1) a core must contain two or more continuous velocity channels, each of which has at least 3 pixels whose intensities are above the 3σ noise level, and (2) the pixels must be connected to one another in both the space and velocity domains. (3) Furthermore, we rejected core candidates located at the edge of the observed region. The total intensity of the minimum mass core identified by this method has about 60σ levels. Using our definition of core mass (eq.[1]), a minimum core mass is estimated to be $0.28 M_\odot$ and $0.38 M_\odot$ for $T_{\text{ex}} = 12\text{ K}$ and 18 K , respectively. The total mass of the identified 68 cores is estimated to be $228 M_\odot$, 60 % of the total mass detected above the 2σ level.

In general, the physical properties of the identified cores depend on the core identification scheme and its parameters. In our case, we expect that our clumpfind can detect the real 3D density structures in the cloud from the H^{13}CO^+ ($J = 1 - 0$) spectral line position-position-velocity data cube because of the following reasons. According to Williams et al. (1994), the physical properties of the cores identified by clumpfind are affected significantly by the adopted threshold and stepsize unless they are carefully chosen. They recommend using the 2σ noise level for both the threshold and stepsize, for which the clumpfind could detect and accurately measure the individual core properties in their test simulations. We adopt this set of the parameters in our clumpfind. Recently, several authors revisited this problem (Pineda et al. 2009; Ikeda & Kitamura 2009). Pineda et al. (2009) reexamined the effect of varying the values of the threshold ($T_{A,\text{th}} = 3, 5,$ and 7σ) and stepsize ($3\sigma \leq \Delta T_A \leq 20\sigma$) for the core identification, and confirmed that the physical quantities of the identified cores depend on these parameters especially when the distribution of the emission is not localized in the data cube and the larger values of the parameters are used

[see also Schneider & Brooks (2004) for the case of the low-spatial resolution (~ 1 pc), optically thick ^{12}CO ($J = 1 - 0$) data with $T_{A,\text{th}} = \Delta T_A = 3 \sigma$]. Ikeda & Kitamura (2009) explored more reasonable parameter ranges of $T_{A,\text{th}} = 2 - 3 \sigma$ and $2 \sigma \leq \Delta T_A \leq 3 \sigma$ suitable for their core study in the OMC-1 region, and demonstrated that the power-law index of a core mass spectrum does not depend on the threshold and stepsize. Williams et al. (1994) also discussed the “overlap” effect for which multiple cores that almost overlap along the line-of-sight are not separately identified by the clumpfind when they have nearly the same line-of-sight velocities. This overlap effect is likely to be significant when the gas is highly turbulent and the emission tends to be distributed in the large volume of the 3D data cube (Ballesteros-Paredes & Mac Low 2002; Smith et al. 2008). For example, Ostriker et al. (2001) performed 3D MHD turbulent simulations and claimed that the emission lines are often singly peaked even in the presence of multiple condensations along the line of sight. We note that their model clouds are highly turbulent, gravitationally unbound and the condensations have extremely large virial ratios, ranging from 10 to 10^3 . This suggests that the overlap effect may be crucial for less dense gravitationally unbound molecular gas components observed by ^{12}CO and ^{13}CO (see Ossenkopf & Mac Low 2002, for the case of the Polaris molecular cloud, a nearby diffuse, gravitationally unbound molecular cloud.). In contrast, for our H^{13}CO^+ data, the overlap effect is expected to be minor because the H^{13}CO^+ emission can trace only dense gas with densities greater than $\sim 10^5 \text{ cm}^{-3}$ and appears to be reasonably localized in the 3D data cube, indicating that the dense gas is likely to have a small volume filling factor in the cloud and moderately quiescent (the Mach number ~ 2). Note that the low density gas has the Mach number of about 5 – 6 (Loren 1989). In fact, our cores have virial ratios of about 2, as shown in §4.5. Thus, we expect that the clumpfind can identify the 3D density structures reasonably well from our H^{13}CO^+ data.

A caveat of our analysis is that the cores identified by the above procedure (and any other core identification schemes) are resolution dependent in the sense that the substructures smaller than the telescope beam size cannot be resolved. It remains unclear whether an identified core is a unit that is separated dynamically from the background media. However, we expect that the structures identified from high density tracers such as H^{13}CO^+ ($J = 1 - 0$), N_2H^+ ($J = 1 - 0$), and dust continuum data correspond to the real dense structures in the cloud as long as the spatial resolution is less than ~ 0.01 pc, because recent numerical simulations of pc-scale cluster forming clumps demonstrated that the dense structures like filaments often created in the clump have sizes of order 0.1 pc or less along the minor axes and densities of order 10^5 cm^{-3} (Li & Nakamura 2006; Nakamura & Li 2007). Therefore, in the following, we discuss the statistical properties of the cores identified by the above procedure, assuming that the identified cores can be regarded as units that are reasonably separated dynamically from the background media. Further investigation of this problem should be done when higher spatial resolution observations are available.

4.2. Derivation of Core Properties

We derive physical properties of the cores using the definitions described in §3.3 of Ikeda et al. (2007). In brief, the position and local standard of rest (LSR) velocity of each core are determined at the pixel with the largest antenna temperature, $T_{A,\text{peak}}^*$, within the core. The core radius, R_{core} , is determined by taking the projected area enclosed by the 2σ level contour and computing the radius of the circle required to reproduce the area, taking into account the correction for the telescope beam ($18''$). The aspect ratio is computed as the ratio of the major to minor axis lengths that are determined by the two-dimensional Gaussian fitting to the total integrated intensity distribution of the core. The FWHM line width, dv_{core} , is corrected for the velocity resolution of the spectrometers ($= 0.13 \text{ km s}^{-1}$) and for line broadening due to hyperfine splitting of H^{13}CO^+ . The LTE mass is estimated as

$$M_{\text{LTE}} = 1.88 \times 10^{-2} \left(\frac{X_{\text{H}^{13}\text{CO}^+}}{1.72 \times 10^{-11}} \right)^{-1} T_{\text{ex}} \exp(4.16/T_{\text{ex}}) \\ \times \left(\frac{D}{125 \text{ pc}} \right)^2 \left(\frac{\Delta\theta}{21''} \right)^2 \left(\frac{\eta}{0.51} \right)^{-1} \left(\frac{\sum_i T_{A,i}^* \Delta v_i}{\text{K km s}^{-1}} \right) M_{\odot}, \quad (1)$$

by assuming that the H^{13}CO^+ emission is optically thin. Here, $X_{\text{H}^{13}\text{CO}^+}$ is the fractional abundance of H^{13}CO^+ relative to H_2 , T_{ex} is the excitation temperature, D is the distance to the ρ Ophiuchi main cloud, $\sum_i T_{A,i}^* \Delta v_i$ is the total integrated intensity of the core and $\Delta v_i = 0.13 \text{ km s}^{-1}$. We adopt the fractional abundance $X_{\text{H}^{13}\text{CO}^+} = 1.72 \times 10^{-11}$ (see §4.3), and the distance $D = 125 \text{ pc}$ on the basis of the values recently updated by Lombardi et al. (2008) and Loinard et al. (2008) (see also Wilking et al. 2008). The excitation temperature is assumed to be $T_{\text{ex}} = 12 \text{ K}$ (Motte et al. 1998) except for the area shown in Figure 2a, i.e., the Oph A region, where $T_{\text{ex}} = 18 \text{ K}$ following the N_2H^+ observations by Di Francesco et al. (2004).

The virial mass M_{vir} is calculated as

$$M_{\text{vir}} = \frac{5a^{-1}R_{\text{core}}dv_{\text{tot}}^2}{8 \ln 2G} \\ = 209a^{-1} \left(\frac{R_{\text{core}}}{\text{pc}} \right) \left(\frac{dv_{\text{tot}}}{\text{km s}^{-1}} \right)^2 M_{\odot}, \quad (2)$$

and

$$dv_{\text{tot}} = \left[dv_{\text{core}}^2 + 8 \ln 2 k_B T \left(\frac{1}{\mu m_H} - \frac{1}{m_{\text{obs}}} \right) \right]^{1/2} \quad (3)$$

where k_B is the Boltzmann constant, T is the kinetic temperature of the molecular gas, μ is the mean molecular weight of 2.33, m_H is the mass of a hydrogen atom, m_{obs} is the mass of a H^{13}CO^+ molecule, and a is a dimensionless parameter of order unity which measures the effects of a nonuniform or nonspherical mass distribution (Bertoldi & McKee 1992). For a uniform sphere and a centrally-condensed sphere with $\rho \propto r^{-2}$, $a = 1$ and $5/3$, respectively. For our cores, the effects of the nonspherical mass distribution appear to be small because the aspect ratios are not

so far from unity (see also Figure 2 of Bertoldi & McKee 1992). The virial ratio, the ratio between the virial mass to the LTE mass, is defined as $\alpha_{\text{vir}} \equiv M_{\text{vir}}/M_{\text{LTE}}$, which is equal to twice the ratio of the internal kinetic energy to the gravitational energy.

The mean number density of the core, \bar{n} , is calculated as the LTE mass divided by the volume of a sphere with radius, R_{core} ,

$$\bar{n} = \frac{3M_{\text{LTE}}}{4\pi\mu m_H R_{\text{core}}^3}. \quad (4)$$

4.3. Fractional Abundance of H^{13}CO^+

To evaluate the fractional abundance of H^{13}CO^+ , we smoothed the 850 μm map with the angular resolution of $21''$ to match the H^{13}CO^+ total integrated intensity map and computed the column densities of H^{13}CO^+ ($N_{\text{H}^{13}\text{CO}^+}$) and H_2 (N_{H_2}) at each pixel in the maps. Here, we computed N_{H_2} from the relation

$$N_{\text{H}_2} = S_{850}^{\text{beam}} / [\Omega_{\text{beam}} \mu m_H \kappa_{850} B_{850}(T)], \quad (5)$$

where S_{850}^{beam} is the 850 μm flux density per beam, Ω_{beam} is the main beam solid angle, $B_{850}(T)$ is the Planck function for a dust temperature T , and κ_{850} ($= 0.01 \text{ cm}^2\text{g}^{-1}$) is the dust opacity at 850 μm (Henning et al. 1995; Ossenkopf & Henning 1994; Johnstone et al. 2000a). The dust temperature is assumed to be equal to the gas temperature. In Figure 4 the fractional abundances $X_{\text{H}^{13}\text{CO}^+}$ computed at all the pixels above the 3σ levels for both the H^{13}CO^+ and 850 μm maps are plotted against N_{H_2} . We note that the H_2 column density derived from the 850 μm map is very sensitive to the temperature and the dust opacity assumed, and therefore have uncertainty of at least a factor of a few. The fractional abundance of H^{13}CO^+ tends to decrease with increasing H_2 column density. The best-fit power-law is given by

$$\log X_{\text{H}^{13}\text{CO}^+} = (-10.87 \pm 0.01) + (-0.514 \pm 0.024) \log(N_{\text{H}_2}/10^{23} \text{ cm}^{-2}) \quad (6)$$

with a correlation coefficient $\mathcal{R} = 0.68$, indicating that $X_{\text{H}^{13}\text{CO}^+}$ is nearly proportional to $N_{\text{H}_2}^{-1/2}$. This tendency is in good agreement with a theoretical consideration of the ionization fraction in molecular clouds if the column density is proportional to the local volume density for each molecule. When the ionization rate by cosmic rays ($\propto n_n$, where n_n is the density of neutral gas) balances with the recombination rate ($\propto n_i n_e$, where n_i and n_e are the densities of positive ion and electron, respectively, and $n_i \approx n_e$), the ionization fraction is inversely proportional to the square root of the neutral gas density (Elmegreen 1979). In typical regions in molecular clouds, the most abundant positive molecular ion is expected to be HCO^+ . Therefore, the fractional abundance of H^{13}CO^+ as well as that of HCO^+ is expected to be inversely proportional to the square root of the neutral gas density if the fractional abundance of H^{13}CO^+ relative to HCO^+ is almost constant. More detailed studies indicate that the relation $X_{\text{H}^{13}\text{CO}^+} \propto n_n^{-1/2}$ is a reasonable approximation of the fractional abundance in the density range of $n \lesssim 10^7 \text{ cm}^{-2}$, although metal ions such as Mg^+ may be the most abundant positive ions (Nishi et al. 1991; Nakano et al. 2002). We note that as mentioned

in §3, in the 850 μm data the structures larger than 1.5' (≈ 0.06 pc) are removed during the data reduction process. To evaluate how the effect of this artificial filtering affects the estimate of the H^{13}CO^+ abundance, we repeated the same analysis by filtering out all the structures larger than 1.5' in the H^{13}CO^+ map and confirmed that the effect of this artificial filtering is negligible. This is because the dense gas detected by the 850 μm and H^{13}CO^+ is spatially well-localized.

In nearby low-mass star forming regions, Butner et al. (1995) found that $X_{\text{H}^{13}\text{CO}^+}$ ranges from 3×10^{-11} to 4×10^{-10} for dense cores with $2 \times 10^{21} \text{ cm}^{-2} \lesssim N_{\text{H}_2} \lesssim 1 \times 10^{22} \text{ cm}^{-2}$, where they estimated the H_2 column densities from C^{18}O ($J = 1-0$) observations. For comparison, their values are indicated by crosses in Figure 4. Although their $X_{\text{H}^{13}\text{CO}^+}$ tends to decrease with increasing N_{H_2} in the same way as for our data, their $X_{\text{H}^{13}\text{CO}^+}$ tend to be somewhat larger than the values predicted from eq. [6]. If $X_{\text{H}^{13}\text{CO}^+}$ derived by Butner et al. (1995) is fitted by a power-law with the same power index as in eq. [6], the coefficient becomes about twice that of eq. [6]. It is difficult, however, to judge whether this difference originates from the different environments because both the data have uncertainty at least by a factor of a few. If both the data are fitted by a power-law with a single index, then the best-fit function is given by

$$\log X_{\text{H}^{13}\text{CO}^+} = (-10.89 \pm 0.01) + (-0.732 \pm 0.014) \log(N_{\text{H}_2}/10^{23} \text{ cm}^{-2}) \quad (7)$$

with $\mathcal{R} = 0.87$. The mean fractional abundance $\langle X_{\text{H}^{13}\text{CO}^+} \rangle$ is estimated to 1.72×10^{-11} with a standard deviation of 0.92×10^{-11} . In the present paper, we assume the constant fractional abundance of $X_{\text{H}^{13}\text{CO}^+} = 1.72 \times 10^{-11}$ for the entire area. In future analysis, the spatial variation in fractional abundance will be taken into account.

van Dishoeck et al. (1995) measured a smaller fractional abundance $X_{\text{H}^{13}\text{CO}^+} \approx 0.75 \times 10^{-11}$ toward IRAS 16293–2422, a young class 0 binary YSO, located in the eastern streamer region of the ρ Ophiuchi molecular cloud complex (see André et al. 2000). They obtained the H_2 column density of $2 \times 10^{23} \text{ cm}^{-2}$ toward this YSO from the C^{17}O observations, somewhat larger than the mean H_2 column density of ρ Oph evaluated from the 850 μm data. Their value, plotted in Fig. 4 by a filled square, is almost on our best-fit power-law of eq. [7]. Thus, we believe that our adopted fractional abundance of 1.72×10^{-11} is a plausible representative value for the ρ Ophiuchi main cloud.

We note that several high-resolution interferometric observations of starless cores in relatively quiescent, low temperature star forming regions like Taurus have revealed that several gas-phase molecules including CO , HCO^+ , and their isotopes tend to deplete at the densities higher than 10^5 cm^{-3} . One might interpret that the decrease in the H^{13}CO^+ abundance with increasing column density is due to the effect of the depletion. However, the effect of the depletion should be small because of the following reasons. In cluster forming regions like ρ Oph, relatively high turbulent motions, protostellar outflows and stellar radiation tend to increase the temperature steadily and/or temporarily, preventing or slowing down the molecular depletion in starless cores. In addition, the high density part where the molecular depletion is significant is spatially localized and therefore the interferometric observations with high spatial resolution are needed to resolve the effect of

depletion in a core. However, our beam size ($\sim 20''$) is not enough to well resolve the structures inside each core (Aikawa et al. 1995). Furthermore, even if the depletion of gas-phase CO and HCO⁺ is significant in ρ Oph, the fractional abundance of HCO⁺ relative to CO does not change with increasing column density because these carbon-bearing molecules tend to equally deplete (Aikawa et al. 1995). In contrast, the H¹³CO⁺ fractional abundances of Butner et al. (1995) and van Dishoeck et al. (1995), for both of which the H₂ column densities are measured from the CO isotopes, do not show such a constant abundance, but decrease significantly with increasing column density, indicating that the dependence of the H¹³CO⁺ abundance on the column density comes from the different physics from the molecular depletion.

4.4. Distribution of Physical Quantities of Dense Cores and Comparison with Dust Cores

In Table 1, we present the physical properties of the 68 identified cores. In Table 2, we summarize the minimum, maximum, mean, and median values of each quantity. The histograms of the radius (R_{core}), LTE mass (M_{LTE}), and mean density (\bar{n}) of the H¹³CO⁺ cores are shown in Figure 5. For comparison, the radius, mass, and mean density of the 850 μm cores listed in Table 7 of Jørgensen et al. (2008) are indicated by the grey histograms in Figure 5. We selected only the 850 μm cores located inside the same observed area as our H¹³CO⁺ map. We also removed cores whose radii are smaller than the SCUBA beam size of $14''$ and corrected the radii of the other cores for the telescope beam size by using eq. [2] of Ikeda et al. (2007). In this procedure, 43 dust cores were selected using the 2σ noise level of $0.04 \text{ Jy beam}^{-1}$. The minimum, maximum, mean, and median values of each quantity of the 850 μm cores are summarized in Table 3. We note that as mentioned in §3, in the 850 μm data the structures larger than $1.5''$ ($\approx 0.06 \text{ pc}$) are removed during the data reduction process and therefore the number of dust cores with radii larger than about 0.03 pc is likely to be underestimated.

The radius of the H¹³CO⁺ cores ranges from 0.022 to 0.069 pc and its distribution has a single peak at around the mean of 0.045 pc (see Figure 5a). The maximum radius of the H¹³CO⁺ cores is only about three times as large as the minimum radius. In other words, most of the cores have similar size. On the other hand, the distribution of the LTE mass is somewhat broad compared with that of the core radius. The LTE mass of the H¹³CO⁺ cores ranges from 0.4 to $22 M_{\odot}$ and its distribution has a single peak at around the mean of $3.3 M_{\odot}$ (see Figure 5b). The maximum mass is about 56 times as large as the minimum. The mean density of the H¹³CO⁺ cores also shows a similar broad distribution, ranging from 3.7×10^4 to $5.8 \times 10^5 \text{ cm}^{-3}$, with a single peak at around the mean density of $1.4 \times 10^5 \text{ cm}^{-3}$ (see Figure 5c).

These distributions of the physical quantities of the H¹³CO⁺ cores are qualitatively similar to those of the 850 μm cores, although the mean radius and mass of the H¹³CO⁺ cores are about twice those of the 850 μm cores. On the other hand, the mean density of the H¹³CO⁺ cores is smaller than that of the 850 μm cores by a factor of 5. This large difference in the mean density

probably comes from the fact that the 850 μm emission tends to trace the higher density parts of the H^{13}CO^+ cores (see Ikeda et al. 2009). Another reason is due to the overlap effect. It is likely that dense cores often overlap one another along the line of sight. Although such overlapped cores can be separated in some degree for the H^{13}CO^+ cores because of their velocity information, such separation is impossible for the two-dimensional clumpfind method that was used for the 850 μm map. In fact, the distribution of the core radius for the 850 μm cores has a tail toward the larger radius. A more prominent tail can be seen in the distribution of the core mass shown in Figure 5b, where the mean core mass is about 2.6 times as large as the median. The tail in the core mass, however, can be caused by the temperature difference. For all the dust cores, the uniform temperature of $T = 15$ K is assumed in Jørgensen et al. (2008). For several massive dust cores, however, the temperatures may be underestimated because they are located in the Oph A region where the temperatures are likely to be higher because of active star formation.

The distribution of the FWHM line width of the H^{13}CO^+ cores are shown in Figure 6. The line width ranges from 0.19 to 0.77 km s^{-1} with a mean of 0.49 km s^{-1} . Following Myers et al. (1991), we classified our cores into two groups: “thermal core” and “turbulent core”, on the basis of the critical line width, dv_{cr} , expressed by

$$dv_{\text{cr}} = \left[8 \ln 2 k_B T \left(\frac{1}{\mu m_H} + \frac{1}{m_{\text{obs}}} \right) \right]^{1/2}. \quad (8)$$

The critical line width of H^{13}CO^+ is estimated to be 0.50 and 0.62 km s^{-1} for $T = 12$ K and 18 K, respectively. Figure 6 indicates that about 40 % of the cores are classified as the turbulent core. However, almost all the turbulent cores have transonic turbulent motions, and highly turbulent cores ($dv_{\text{core}} \gtrsim 1 \text{ km s}^{-1}$) found in massive star forming regions such as Orion A (Ikeda et al. 2007) are not seen in the ρ Ophiuchi main cloud.

4.5. Comparison Between Cores with and without YSOs

Recent observations of the Ophiuchi molecular cloud complex with the Spitzer Space Telescope (Padgett et al. 2008) allow us to compare the physical properties of H^{13}CO^+ cores associated with and without YSOs (Jørgensen et al. 2008). Previous studies have suggested that the physical properties of dense cores associated with YSOs are different from those of cores without YSOs (e.g., Benson & Myers 1989; Jijina et al. 1999; Walsh et al. 2007). Based on the spectral indices at the near- and mid-infrared wavelengths, Jørgensen et al. (2008) classified YSOs in L1688 into 4 classes that represent the following evolutionary stages of YSOs: Class I, Flat Spectrum, Class II, and Class III. We use their YSO catalog to identify the H^{13}CO^+ cores with YSOs. We note that in their classification, the Class 0 YSOs, the youngest objects, are included in Class I. For example, the prototypical Class 0 object, VLA 1623, is classified as Class I in their list.

The spatial distribution of the YSOs is shown in Figure 7, which indicates that the distribution of the Class I and Flat Spectrum sources follows that of the H^{13}CO^+ ($J = 1 - 0$) emission. On

the other hand, more evolved YSOs, the Class II and III sources, tend to be distributed in the entire observed area with no strong correlation with the distribution of the H^{13}CO^+ ($J = 1 - 0$) emission. Therefore, we expect that the Class I and Flat Spectrum sources are probably embedded in the dense gas, and use the two classes of YSOs to divide the H^{13}CO cores into the following two groups: protostellar and starless cores. If either a Class I or Flat Spectrum object is located within the extent of a H^{13}CO^+ core, we regard the core as a protostellar core. The others are classified as starless cores, even if Class II or III sources are located within the cores. In this classification, a Class I or Flat Spectrum source is sometimes located within the extents of two or more cores which partly overlap one another along the line of sight. We classified all such cores as protostellar cores because we have no information on the line of sight velocities of the YSOs. Therefore, the number of protostellar cores is likely to be overestimated. According to the above procedure, we found 34 protostellar and 34 starless cores.

Figure 8 compares the physical properties of the starless and protostellar cores. The minimum, maximum, mean, and median values are summarized in Table 4. The radii (Figures 8a) and masses (Figures 8b) of the protostellar cores tend to be larger than those of the starless cores. In particular, the mean LTE mass of the protostellar cores is about twice as large as that of the starless cores. These results are consistent with those of the N_2H^+ cores in NGC1333 (Walsh et al. 2007) and the H^{13}CO^+ cores in Orion A (Ikeda et al. 2007).

The line widths of the protostellar cores tend to be larger than those of the starless cores (Figures 8c). A similar tendency is seen in the NH_3 cores observed by Benson & Myers (1989) and Jijina et al. (1999), who interpreted that stellar winds and protostellar outflows create local turbulence. If stellar winds and protostellar outflows enhance internal turbulent motions for the protostellar cores, such cores must have had virial ratios smaller than the current values in the prestellar phase. Although the distribution of the virial ratios for the protostellar cores appears to be broader than that of the starless cores, there seems to be no significant difference in the virial ratio between the protostellar and starless cores (Figures 8d): for both the starless and protostellar cores, the virial ratio has a mean of about 2 – 3, ranging from 0.4 to 8. Here, the dimensionless parameter a in eq.[2] is adopted to be unity, the value of a uniform sphere, for both the starless and protostellar cores. If for protostellar cores, the value of a centrally condensed density distribution, $a = 5/3$, is adopted, the virial ratios of the protostellar cores tend to be somewhat smaller than those of the starless cores that are expected to have flattened density distributions. This appears to contradict the idea that outflows enhance the virial ratios of the parent cores. About 60 % of the cores have virial ratios smaller than 2, for which the net internal energies are negative. Therefore, we conclude that the majority of the cores are likely to be self-gravitating.

Figure 8e shows that the distributions of the mean densities of the protostellar and starless cores are similar to each other, although some of the protostellar cores have very large densities. Figure 8f indicates that the starless cores tend to have larger aspect ratios than those of the protostellar cores. For example, for the starless cores, 5 (15%) out of 34 have aspect ratios larger than 2, whereas for the protostellar cores, no cores have such large aspect ratios. The starless cores

with aspect ratios larger than 2 have large virial ratios ($\alpha_{\text{vir}} \gtrsim 3$) and are likely to be gravitationally unbound.

4.6. Correlation among Physical Properties of Dense Cores

4.6.1. Line Width-Radius and Mass-Radius Relations

The line width measured from molecular line emission provides us with information on kinetic properties such as thermal motion and turbulence. Based on data in the literature, Larson (1981) found that the line width of molecular clouds and cores is well correlated with the radius and mass, and the correlations are approximately of power-law form. He suggested that the power-law relations stem from processes of interstellar turbulence cascade. The strong correlations of the power-law relations also suggest that the molecular clouds and cores are nearly in virial equilibrium. Since his pioneering work, many studies have been carried out to investigate the dependence of the line width on its radius for various molecular clouds and cores using different molecular emission lines (e.g., Sanders et al. 1985; Dame et al. 1986; Heyer & Brunt 2004). Observations based mainly on low-density tracers such as ^{12}CO ($J = 1 - 0$) and ^{13}CO ($J = 1 - 0$) have generally supported Larson’s idea (e.g., Myers 1983; Fuller & Myers 1992). In contrast, observations based on higher-density tracers such as C^{18}O , CS, and H^{13}CO^+ have often shown that the dependence of the line width on its radius tends to be very weak (e.g., Tachihara et al. 2002; Ikeda et al. 2007, 2009; Saito et al. 2008). For massive star forming regions, the shallower power-law relations have also been found (Caselli & Myers 1995; Plume et al. 1997).

The line width-radius relation for the identified cores is presented in Figure 9a. The filled squares and open circles indicate the starless and protostellar cores, respectively. As mentioned in §4.5, the protostellar cores tend to have larger line widths and larger radii than those of the starless cores. Such a tendency can be recognized in Figure 9a. The best-fit power-law for all the cores is given by

$$\log(dv_{\text{core}}/\text{km s}^{-1}) = (0.319 \pm 0.179) + (0.478 \pm 0.131) \log(R_{\text{core}}/\text{pc}) , \quad (9)$$

with $\mathcal{R} = 0.410$. As representative examples, the line width-radius relations derived by Larson (1981) and Heyer & Brunt (2004) are also plotted in Figure 9a with the dotted and dashed lines, respectively. Heyer & Brunt (2004) applied the Principal Component Analysis to derive the line width-radius relation inside molecular clouds from ^{12}CO observations. The line widths of the H^{13}CO^+ cores tend to be significantly larger than those of the Heyer & Brunt relation and somewhat smaller than those of the Larson relation. We note that the line widths of the Larson relation tend to be larger over the scale 0.01 – 0.1 pc compared to the line width-radius relations derived by other authors (e.g., Solomon et al. 1987; Myers 1983) and thus may correspond to the upper bound of the relations. Although the power index of our cores is not far from those of Larson (1981) and Heyer & Brunt (2004), the correlation is very weak. Such a weak correlation is also seen for the H^{13}CO^+ cores in Orion A (Ikeda et al. 2007). In §5 we will discuss the line width-radius relation

of the H^{13}CO^+ cores in more detail.

To separate the turbulent motion from the thermal motion within each core, we plot in Figure 9b the nonthermal line width $dv_{\text{NT}}[\equiv (dv_{\text{tot}}^2 - 8 \ln 2 k_B T / \mu m_H)^{1/2}]$ against core radius. The best-fit power-law for all the cores, shown by the solid line in Figure 9b, is given by

$$\log(dv_{\text{NT}}/\text{km s}^{-1}) = (0.501 \pm 0.218) + (0.634 \pm 0.159) \log(R/\text{pc}) \quad (10)$$

with $\mathcal{R} = 0.440$. For comparison, the nonthermal line width-radius relation for low-mass cores compiled by Caselli & Myers (1995), $(dv_{\text{NT}}/\text{km s}^{-1}) = 1.2(R/\text{pc})^{0.53}$, is indicated by the dashed line, where we replaced the radius of Caselli & Myers (1995) (R_{CM}) by the radius of our definition. See the Appendix in detail. Although our relation has a power-law index similar to that of Caselli & Myers (1995), the coefficient is somewhat larger. This suggests that turbulence within our cores is not as much dissipated as the Caselli & Myers relation predicts. This tendency is different from that of the H^{13}CO^+ cores in Orion A where the $dv_{\text{NT}}-R_{\text{core}}$ relation agrees well with the Caselli & Myers relation (Ikeda et al. 2007). In §5 we will compare our cores with the Orion A cores and discuss this point in more detail.

Recently, Volgenau et al. (2006) attempted to measure the relationship between the line width and size inside three protostellar cores having multiple protostars in the Perseus molecular cloud, using the Regions-Of-Contrast (ROC) analysis proposed by Ostriker et al. (2001). Our line width-radius relation is essentially different from that derived from the ROC analysis, and therefore, it is difficult to directly compare the two relations. In the ROC analysis, the size is just a region size that is not related to a dense core. When the ROC analysis is applied to substructures inside a core, the line width-size relation tends to have a large scatter, especially when the objects have complicated structures like those observed by Volgenau et al. (2006), in which the disk rotation, disk instability, and stellar feedback such as stellar winds and outflows influence the local structures significantly. In contrast, in our analysis, the size (or radius) corresponds to that of an identified core. Therefore, the relatively large scatter in our line width-radius relation is likely to reflect the difference in the dynamical states of the cores (see also §5.2). In fact, recent numerical simulations of turbulent molecular clouds demonstrated that the cores identified directly from the 3D density distribution are in various dynamical states and show similar large scatter in the line width-radius relation (Nakamura & Li 2008; Offner et al. 2008).

In Figure 9c, we plot the LTE mass against core radius. The best-fit power-law is given by

$$\log(M_{\text{LTE}}/M_{\odot}) = (3.95 \pm 0.34) + (2.64 \pm 0.25) \log(R_{\text{core}}/\text{pc}) \quad (11)$$

where $\mathcal{R} = 0.790$. For comparison, the relation of $M_{\text{LTE}} = 4\pi\mu m_H \bar{n} R_{\text{core}}^3 / 3$ is indicated by the dashed line in Figure 9c, where $\bar{n} = 1.35 \times 10^5 \text{ cm}^{-3}$. The power-law index of ~ 3 indicates that the mean density of each core is comparable to the critical density of H^{13}CO^+ ($J = 1 - 0$), $n_{\text{cr}} \simeq 8 \times 10^4 \text{ cm}^{-3}$. The coefficient of our $M_{\text{LTE}}-R_{\text{core}}$ relation is an order of magnitude larger than that of Larson (1981), which is mainly based on ^{13}CO ($J = 1 - 0$) whose critical density is about 10^3 cm^{-3} . This tendency is in good agreement with that of the Orion A cores (Ikeda et al. 2007, 2009).

4.6.2. Virial Ratio

The boundedness of a core is often estimated using the virial ratio. In Figure 10, we plot against LTE mass the virial ratio calculated using eq.[2], where for both the protostellar and starless cores a dimensionless parameter a is set to unity, the value of a uniform sphere. The best-fit power-law of our cores is given by

$$\log \alpha_{\text{vir}} = (0.528 \pm 0.018) + (-0.600 \pm 0.057) \log(M_{\text{LTE}}/M_{\odot}) \quad (12)$$

with $\mathcal{R} = 0.817$. The virial ratio tends to increase with decreasing the LTE mass, and has a mean of 2.4, ranging from 0.4 to 8. More than a half the cores have virial ratios smaller than 2 and thus the majority of the cores are more or less self-gravitating. According to Bertoldi & McKee (1992), a self-gravitating core confined by ambient pressure has a virial ratio of $\alpha_{\text{vir}} = 2.06(M_{\text{LTE}}/M_J)^{-2/3}$, where M_J is the Jeans mass defined by eq. [2.13] of Bertoldi & McKee (1992). For comparison, the virial ratio of a self-gravitating core confined by ambient pressure is plotted by the dashed line in Figure 10. Here, using the velocity dispersion of 0.35 km s^{-1} and the ambient gas density of 10^5 cm^{-3} (see the derivation of these values in §5), the Jeans mass is estimated to be about $2.4 M_{\odot}$, almost equal to the median mass of the identified cores. The best-fit power-law is very close to the virial ratio of a self-gravitating core confined by ambient pressure. The virial ratios of the identified cores tend to be, however, smaller than that of a non self-gravitating, pressure-confined core with $\alpha_{\text{vir}} = 2.9(M_{\text{LTE}}/M_J)^{-2/3}$, for a given core mass (Bertoldi & McKee 1992). Therefore, for our cores, both the self-gravity and ambient pressure play an important role in dynamics of the cores. In §5 we will discuss the dynamical states of our cores in more detail.

5. Discussion

5.1. Core Mass Spectrum in the ρ Ophiuchi Main Cloud

The mass spectrum of our cores is plotted in Figure 11. The core mass spectrum appears to be fitted by a two-component power-law. There seems to be a break at around $7M_{\odot}$, about twice the mean LTE mass of $3.4M_{\odot}$. Above the break, the mass spectrum is steeper, while below the break, it is flattened. The mass spectrum can be fitted by the following two-component power-law:

$$dN/dM \propto M^{-0.43 \pm 0.03} \text{ for } M_{\text{LTE}} \lesssim 7M_{\odot} \quad (13)$$

$$\propto M^{-2.4 \pm 0.3} \text{ for } M_{\text{LTE}} \gtrsim 7M_{\odot} . \quad (14)$$

This mass spectrum is broadly consistent with those of the dust cores in ρ Oph, although for the dust cores the low-mass parts are somewhat steeper and the break masses are smaller (Motte et al. 1998; Johnstone et al. 2000a; Stanke et al. 2006; Stamatellos et al. 2007; Enoch et al. 2008; Simpson et al. 2008). For example, Stamatellos et al. (2007) revised the mass spectrum of the dust cores identified by Motte et al. (1998) by reestimating the dust temperatures. The revised mass spectrum is fitted

by a two-component power-law with a low-mass index of -1.5 , a high-mass index of -2 , and a break at around $1M_{\odot}$. Simpson et al. (2008) reanalyzed the SCUBA $850 \mu\text{m}$ archive data and obtained the core mass spectrum that can be fitted by a three-component power-law with a low-mass index of -0.7 , intermediate-mass index of -1.3 , high-mass index of -2.35 , and two breaks at around $0.7M_{\odot}$ and $2M_{\odot}$. We note that the slopes and the break masses of the core mass spectra are affected by the number of bins, if it is not appropriately set (Rosolowsky 2005). Thus, the cumulative form of the core mass spectra is sometimes used when the number of cores is small, although it requires a more complicated uncertainty analysis (see e.g., Reid & Wilson 2006). As for the parameters of the clumpfind, the slopes are almost independent of the threshold and stepsize of the clumpfind as long as they are appropriately set (Ikeda & Kitamura 2009). For the core mass spectra mentioned above, the difference in the break mass is likely to come from the fact that the H^{13}CO^+ emission traces more extended, less dense structures than the dust continuum emissions. The break mass may also be affected by the “confusion” which means the situation that multiple cores with similar v_{LSR} are overlapped along the same line of sight and therefore cannot be separated into individual cores using the clumpfind (see Ikeda et al. 2007, 2009).

Based on the ISOCAM observations, Bontemps et al. (2001) identified over 200 YSOs in ρ Oph and derived the mass function of 123 Class II YSOs that is well fitted by a two-component power-law with a low-mass index of -1.15 , a high-mass index of -2.7 , and a break at around $0.55M_{\odot}$. The mass spectrum of the H^{13}CO^+ cores is roughly similar in shape to the stellar IMF in ρ Oph, although the slopes in the low mass and high mass parts of the H^{13}CO^+ core mass spectrum are somewhat shallower and the break mass is one order of magnitude larger.

5.2. Dynamical State of H^{13}CO^+ Cores in the ρ Ophiuchi Main Cloud

Virial theorem is useful for analyzing the dynamical states of dense cores. The virial equation for a uniform spherical core is given by

$$\frac{1}{2} \frac{\partial^2 I}{\partial t^2} = U + W + S \quad (15)$$

where the terms, I , U , W , and S , denote the moment of inertia, internal kinetic energy, gravitational energy including the effect of magnetic field, and surface pressure, respectively, and are given as follows (Nakano 1998):

$$U = \frac{3Mdv_{\text{tot}}^2}{8 \ln 2} \quad (16)$$

$$W = -\frac{3GM^2}{5R_{\text{core}}} \left[1 - \left(\frac{\Phi}{\Phi_{\text{cr}}} \right)^2 \right] \quad (17)$$

$$S = -4\pi R^3 P_{\text{ex}} . \quad (18)$$

The values Φ and Φ_{cr} are, respectively, the magnetic flux penetrating the core and the critical magnetic flux above which the magnetic field can support the core against the self-gravity. Here,

the core is assumed to have condensed from much lower density medium and the radius of the magnetic flux tube penetrating the core is much smaller than that before contraction [see §2 of Nakano (1998)]. P_{ex} is the surface pressure including both thermal and turbulent components. M is the core mass and is chosen to be the LTE mass of the core.

All the above terms in the virial equation except P_{ex} and Φ can be estimated from the physical quantities listed in Table 1. It is difficult to estimate the surface pressures exerted on individual cores directly from our data. Instead of deriving the surface pressures of individual cores, we adopt a representative surface pressure from the average densities and velocity dispersions that were measured in subclumps Oph A, B, C, E, and F: $\langle P_{\text{ex}} \rangle \approx \langle \rho \rangle \langle \sigma \rangle^2$. Here, $\langle \rho \rangle$ is the average density and $\langle \sigma \rangle$ is the average velocity dispersion including both the thermal and turbulent components as $\langle \sigma \rangle^2 = \langle \sigma_{\text{NT}} \rangle^2 + c_s^2$, where $\langle \sigma_{\text{NT}} \rangle$ and c_s are the velocity dispersion of the nonthermal component and the isothermal sound speed, respectively. The average density and velocity dispersion were evaluated as $\langle \rho \rangle / (2.33m_H) \approx (0.5 - 1) \times 10^5 \text{ cm}^{-3}$ and $\langle \sigma \rangle \approx 0.3 - 0.4 \text{ km s}^{-1}$, respectively. The average surface pressure is then given by $\langle P_{\text{ex}} \rangle / k_B \approx 3 \times 10^6 \text{ K cm}^{-3}$. This value is about a few times as large as the thermal pressure [$\approx 10^5 \text{ cm}^{-3} \times (12 - 18) \text{ K} \approx (1 - 2) \times 10^6 \text{ K cm}^{-3}$]. In the following, we adopt the above $\langle P_{\text{ex}} \rangle$ as a representative value for our cores. This surface pressure is about a half the average internal pressure inside the cores ($\approx 6 \times 10^6 \text{ K cm}^{-3}$) and close to the lower limit of the critical ambient pressure for the dust cores obtained by Johnstone et al. (2000a).

On the other hand, there is only one reliable measurement of the magnetic field strength toward the ρ Ophiuchi main cloud. Crutcher et al. (1993) performed OH Zeeman effect measurements toward two positions in ρ Oph with a beam size $18'$. For one of the two positions that well covers the entire observed area of our data, they derived the line-of-sight magnetic field strength of about $10 \mu\text{G}$ at the low density cloud envelope of $N_{\text{H}_2} \approx 5 \times 10^{21} \text{ cm}^{-3}$ (see also Troland et al. 1996). Based on this measurement, Crutcher (1999) estimated the magnetic flux normalized to the critical value to be $\Phi/\Phi_{\text{cr}} \simeq 0.4$. If we adopt this value as a representative value of Φ/Φ_{cr} for our cores, the magnetic effect is likely to be minor: it reduces the gravitational energy term only by 16%. However, recent turbulent simulations have demonstrated that cores formed out of turbulent clouds can have much larger values of Φ/Φ_{cr} than the cloud initial values (e.g., Dib et al. 2007) and thus it is very difficult to assess the values of Φ/Φ_{cr} for the individual cores without direct measurements of the magnetic fields associated with the cores. In the following, we simply assume $\Phi/\Phi_{\text{cr}} = 0$.

The equilibrium line, $U + W + S = 0$, is shown by the solid line in Fig. 12, where the surface term (S) is plotted against the gravitational energy term (W), both normalized to the internal energy term (U). For the cores that lie below the solid line, the value of $U + W + S$ is negative and thus expected to be bound. All the others are unbound and expected to disperse away, if they do not gain more mass through accretion and/or merging with other cores, or reduce internal support through turbulence dissipation. More than a half the cores lie below the equilibrium line, and are thus bound: they are expected to collapse and form stars. This is also true even in the presence of magnetic field as long as the magnetic flux does not exceed about a half the critical value. Furthermore, the majority of the cores lie below the line of $S = W$ (dashed line), indicating

that the surface term is more important than the gravitational energy term. Even for the cores lying above the line $S = W$, the surface pressure appears to be dynamically important for almost all such cores because the deviation from the line is small. We note that this plot should be valid statistically, but for any individual points the true surface pressures could be higher or lower than the representative surface pressure.

Our virial analysis indicates that the formation and evolution of dense cores in the cluster environment are likely to be strongly influenced by the external compression due to local turbulent motions (see also Dobashi et al. 2001 for importance of external pressures at cloud scales). Such local compression may be responsible for the formation of binary and multiple stars or formation of substellar objects (brown dwarfs or planetary mass objects) in each core under the cluster environment (Hennebelle et al. 2003; Gomez et al. 2007; Whitworth et al. 2007).

5.3. Comparison with Orion A

The Orion A molecular cloud is the nearest giant molecular cloud located at a distance of 480 pc (Genzel et al. 1981), about 4 times as distant as the ρ Ophiuchi main cloud. Recently, Ikeda et al. (2007) carried out the H^{13}CO^+ ($J = 1 - 0$) core survey in the whole region of Orion A using the Nobeyama 45 m telescope and identified 236 cores by the same method as adopted in the present paper. Their core sample is ideal for comparison with our cores because the same molecular emission line, the same telescope, and the same core identification procedure are used. In this subsection, we compare the physical properties of our cores in ρ Oph with those in Orion A.

Figures 13 and 14 compare the physical properties of the ρ Oph cores with those of the Orion A cores. The open squares and crosses indicate the ρ Oph cores and the Orion A cores, respectively. The mean radius of the ρ Oph cores, 0.045 pc, is about three times smaller than that of the Orion A cores, 0.14 pc. This probably reflects the different spatial resolutions (or different distances) for both the observations. In fact, the area where the ρ Oph cores are distributed is well separated from that of the Orion A cores on the plots of the line width-radius and mass-radius relations (see Figure 13). On the other hand, the mean mass of the ρ Oph cores, $3.35 M_{\odot}$, is only about 3.6 times smaller than that of the Orion A cores, $12 M_{\odot}$. This is because the mean density of the Orion A cores, $1.6 \times 10^4 \text{ cm}^{-3}$, is much smaller than that of the ρ Oph cores, $1.4 \times 10^5 \text{ cm}^{-3}$. In particular, the mean density of the Orion A cores is smaller than the critical density of the H^{13}CO^+ ($J = 1 - 0$), $8 \times 10^4 \text{ cm}^{-3}$, and therefore the Orion A cores are likely to contain substructures that could not be spatially resolved.

The mean line width of the ρ Oph cores, 0.488 km s^{-1} , is almost the same as that of the Orion A cores, 0.52 km s^{-1} , in spite of the different core radii. The ranges of the line widths are also similar to each other (see Figure 13). On the other hand, the virial ratio of the Orion A cores seems three times larger than that of the ρ Oph cores for a given LTE mass, as shown in Figure 14. This

difference may be explained also by the different spatial resolutions as follows. The virial ratio is proportional to both the radius and the square of the line width for a given LTE mass. Since the line widths of both the cores are comparable to each other and the radii of the Orion A cores are roughly three times larger than those of the ρ Oph cores, the virial ratio of Orion A becomes three times larger than that of ρ Oph for a given LTE mass.

To elucidate whether or not the different spatial resolutions dominate the different core properties in the two clouds, we try to eliminate the effect of the different spatial resolutions as follows. We smoothed the original ρ Oph data on a coarser grid with a grid spacing of $80''$ by convolving with a 2D Gaussian kernel with a FWHM of $80''$ in the α - δ space. The smoothed data correspond to the data that would be observed by the Nobeyama 45 m telescope if the ρ Ophiuchi main cloud were located at the same distance as the Orion A molecular cloud. Then, applying the clumpfind to the smoothed data, we reidentified 16 dense cores, which are plotted by the filled circles in Figures 13 and 14. In Figures 13a and 13b, the ρ Oph cores identified from the smoothed data are located just in the areas where the Orion A cores are distributed. In contrast, the virial ratios of the reidentified ρ Oph cores are somewhat smaller than those of Orion A for a given LTE mass (see Figure 14a). The larger virial ratios for the Orion A cores may reflect the larger $X_{\text{H}^{13}\text{CO}^+}$ adopted by Ikeda et al. (2007), 4.8×10^{-11} , which is derived using the ^{13}CO abundance measured in the cloud envelope of Taurus, which has much lower column densities than Orion A. If we use the ^{13}CO abundance obtained by Frerking et al. (1982) for ρ Oph, which has column densities comparable to the region observed by Ikeda et al. (2007), the H^{13}CO^+ abundance is reduced by a factor of 2, close to our value. Note that our value is in agreement with that of Ikeda et al. (2007) within uncertainty mentioned by them. Using our value of $X_{\text{H}^{13}\text{CO}^+}$, the distribution of the Orion A cores in the virial ratio-LTE mass plot becomes consistent with that of the ρ Oph cores identified from the smoothed data, as presented in Figure 14b. Although in that case, the LTE masses of the Orion A cores shift upward in Figure 13b, the distributions of the ρ Oph and Orion A cores in the LTE mass-radius relation plot are still well overlapped with each other. Therefore, we conclude that there are no clear differences in the core properties between the ρ Oph and Orion A clouds. The apparent differences in the core properties between the two clouds are likely to be caused mainly by the different spatial resolutions.

5.4. Line Widths of the H^{13}CO^+ cores and Implication for Turbulent Generation

Figure 13 shows that there are no highly turbulent cores having $dv_{\text{core}} \gtrsim 1 \text{ km s}^{-1}$ in ρ Oph. According to Ikeda et al. (2007), all the highly turbulent cores in Orion A are located within 1 pc from the M42 HII region and are probably influenced greatly by the nearby OB stars. The turbulent cores are expected to be responsible for massive star formation (see the discussion of §4.3 of Ikeda et al. 2007). The absence of such highly turbulent cores in ρ Oph may imply that massive O stars will not form in ρ Oph under the current environment.

It is also interesting that the range of the line widths of the ρ Oph cores identified from the

smoothed data almost coincide with that of the original ρ Oph cores. If we fit a single power-law to both the ρ Oph cores identified from the original and smoothed data, the best-fit result becomes $dv_{\text{core}} = (0.599 \pm 0.104) R_{\text{core}}^{0.073 \pm 0.060}$ with a very small correlation coefficient of 0.137, which is shown by the solid line in Figure 13. In other words, the line width appears to be almost independent of the core radius. Since the cores identified from the smoothed data contain adjacent several cores identified from the original data, the nearly independent relationship between the line width and core radius, or the nearly flat line width-radius relation, suggests that the inter-core motions among the neighboring cores are almost comparable to the internal motions in the individual cores. Such a feature is pointed out by André et al. (2007) who measured the velocity difference among the neighboring cores from the centroid velocities of the cores observed by N_2H^+ ($J = 1 - 0$). If the line width-radius relation is flat ($dv_{\text{core}} \approx \text{const.}$) and the core mass is proportional to R_{core}^3 , then the virial ratio is scaled as $\alpha_{\text{vir}} \propto R_{\text{core}} dv_{\text{core}}^2 / (GM_{\text{LTE}}) \propto M_{\text{LTE}}^{-2/3}$, a similar power-law to that derived by Bertoldi & McKee (1992). This again suggests the importance of ambient turbulent pressure in dynamics of the cores as discussed in §5.2.

The line width-radius relation of the ρ Oph cores appears to be inconsistent with one of the most reliable measurements of the line width-size relation, recently obtained by Heyer & Brunt (2004), who found a strong correlation between the line width and size based on the ^{12}CO observations toward 27 nearby giant molecular clouds, despite the large differences in cloud environments and local star formation activity. Their relation, plotted by the dashed line in Figure 13 [$(dv/\text{kms}^{-1}) = 1.1(R/\text{pc})^{0.65}$], leads to the interpretation that most of the turbulent energy comes from the largest scale that is comparable to the cloud size (see the Appendix). Heyer & Brunt (2007) claimed that the driving mechanisms of turbulence at small scales such as protostellar outflows and stellar winds may not play an important role in dynamics of molecular clouds. The FWHM line width ($\Delta V \sim 1.5 \text{ km s}^{-1}$) and radius ($R \sim 1.5 \text{ pc}$) measured from the ^{13}CO ($J = 1 - 0$) line toward the whole ρ Ophiuchi main cloud are in good agreement with the Heyer & Brunt relation. In contrast, the ρ Oph cores identified from the original data tend to deviate upwards from the Heyer & Brunt relation. The nearly flat line width-radius relation of the ρ Oph cores may also suggest that turbulent energy has been injected at the scales smaller than $R \sim 0.35 \text{ pc}$, at which our best-fit power-law intersects with the Heyer & Brunt relation. This scale is in reasonable agreement with the characteristic length scale of the outflow-driven turbulence estimated from the theoretical consideration (Matzner 2007; Nakamura & Li 2007). Based on ^{13}CO and C^{18}O observations, Swift & Welch (2008) derived a similar characteristic scale of the outflow-driven turbulence of $\approx 0.05 \text{ pc}$ toward L1551. However, the universality of the Heyer & Brunt relation implies that the outflow-driven turbulence may be limited to the localized dense regions where active star formation occurs. A caveat is that it is unclear whether the Heyer & Brunt relation, based on the ^{12}CO observations, is still applicable to dense gas where stars are forming. Therefore, the deviation of the line widths for ρ Oph from the Heyer-Brunt relation may be apparent. However, it is worth noting that the nearly flat line width-radius relation is consistent with the virial ratio-mass relation of the pressure-confined, self-gravitating cores ($\alpha_{\text{vir}} \propto M^{-2/3}$). This may suggest that the characteristic length scale of 0.35 pc is related to the formation of dense self-gravitating structures. In any case, if such a small scale

driving of turbulence is common in the cluster environment, star formation in clusters is likely to continue over several dynamical times.

On the other hand, the line widths of our cores deviate downward from the Larson relation which may correspond to the upper bound of the observed line width-radius relations. Until now, many authors have derived the line width-radius relations for various molecular clouds and cores. Those studies show a scatter in the index and coefficient of the power-law line width-radius relations. The line widths of the Larson relation, $(\Delta v/\text{kms}^{-1}) = 1.9(R/\text{pc})^{0.38}$, tend to be somewhat larger over the range of 0.01 – 0.1 pc compared to the other relations and thus may correspond to the upper bound of the relations. For example, on the basis of the Massachusetts-Stony Brook Galactic Plane Survey data, Solomon et al. (1987) derived the relation of $(\Delta v/\text{kms}^{-1}) = 2.1(R/\text{pc})^{0.5}$, not far from the Heyer & Brunt relation. In nearby low-mass star forming regions Fuller & Myers (1992) compiled the data of dense cores and derived the power-law relation of $(\Delta v/\text{kms}^{-1}) = 1.0(R/\text{pc})^{0.4}$ for starless cores. If the line width-radius relation of the low-density gas in ρ Oph follows the Larson relation, instead of the Heyer & Brunt relation, the smaller line widths of the H^{13}CO^+ cores may suggest that the cores have formed preferentially in regions where supersonic turbulence dissipated and thus the cores so formed have smaller line widths compared to the Larson relation. If this is the case, the nearly independent relationship between the line width and core radius implies that the turbulent field at the small scales has not been relaxed yet, and therefore the timescale of core formation may be of the order of a dynamical time. In that case, it is unclear how protostellar outflows contribute to maintain supersonic turbulence in the cluster environment.

6. Summary

Using the archive data of the H^{13}CO^+ ($J = 1 - 0$) molecular line emission taken with the Nobeyama 45 m radio telescope, we analyzed the molecular gas distribution in the central dense region of the ρ Ophiuchi main cloud. We summarize the primary results of the paper as follows:

1. We compared the global distribution of the H^{13}CO^+ emission with that of the 850 μm dust continuum emission and found that the overall spatial distributions are similar to each other, while the H^{13}CO^+ emission appears to cover a larger area than the dust continuum emission. By comparing between the H^{13}CO^+ and 850 μm maps, we revealed that the fractional abundance of H^{13}CO^+ relative to H_2 decreases with increasing the H_2 column density as $X_{\text{H}^{13}\text{CO}^+} \propto N_{\text{H}_2}^{-1/2}$. This tendency is consistent with the theoretical prediction (e.g., Nakano et al. 2002). The mean fractional abundance in the region is estimated to be 1.72×10^{-11} .

2. From the 3D data cube of the H^{13}CO^+ emission we identified 68 dense cores using the clumpfind method. From comparison with the positions of YSOs recently identified by the Spitzer space telescope, the cores are classified into the following two groups: 34 protostellar and 34 starless cores. The radii, masses, and line widths of the protostellar cores tend to be larger than those of the starless cores. The virial ratio tends to increase with decreasing the LTE mass, although we found

no significant difference in the virial ratio between the protostellar and starless cores. Furthermore, the virial ratios of the cores can be well described by the model of a self-gravitating core confined by ambient pressure derived by Bertoldi & McKee (1992), suggesting that both self-gravity and ambient pressure play an important role in dynamics of the cores.

3. The mass spectrum of the H^{13}CO^+ cores can be fitted by a two-component power-law that resembles the stellar IMF in ρ Oph. The core mass spectrum has a break at around $7M_{\odot}$, close to the mean LTE mass of the cores. It implies that the stellar IMF may be at least partly determined by the core mass distribution.

4. Applying the virial analysis, we conclude that most of the cores are bound and are expected to collapse. Furthermore, for the majority of the cores, the surface pressure term is more important than the gravitational energy term. This result suggests that in the cluster environment the formation and evolution of the cores may be regulated largely by the surface pressures.

5. We compared the physical properties of the H^{13}CO^+ cores in ρ Oph with those in Orion A. To eliminate the effect of the different distances, we smoothed the original ρ Oph data into a coarser grid so that the spatial resolutions coincide with each other. We identified 16 cores from the smoothed data using the clumpfind. These cores would be observed by the Nobeyama 45 m telescope if the ρ Ophiuchi main cloud were located at the same distance as the Orion A molecular cloud. The physical properties of the ρ Oph cores identified from the smoothed data appear to resemble those of Orion A. The fact that the mean density of the Orion A cores ($1.6 \times 10^4 \text{ cm}^{-3}$) is somewhat smaller than the critical density of H^{13}CO^+ ($J = 1 - 0$) transition of $8 \times 10^4 \text{ cm}^{-3}$ suggests that the Orion A cores contain clumpy substructures that could not be spatially resolved.

6. The range of the line widths of the ρ Oph cores identified from the smoothed data almost coincides with that of the original ρ Oph cores. This suggests that the line width-radius relation is more or less flat over the range of $0.01 - 0.1$ pc for the dense gas detected by H^{13}CO^+ . Such a flat relation is inconsistent with that derived from the ^{12}CO observations by Heyer & Brunt (2004) who found that the line width correlates strongly with the size for the low-density molecular gas. At the scales below 0.3 pc, the line widths of the ρ Oph cores deviate upwards from the Heyer & Brunt relation. This may be due to turbulence driven by protostellar outflows. However, if the actual line widths of the low-density gas in ρ Oph agree with the values of the Larson relation, then the nearly independent relationship between the line width and core radius may be interpreted as evidence that the cores have formed preferentially in regions where supersonic turbulence dissipated.

A. Comparison with Other Line Width-Radius Relations

In the present paper, the FWHM line width and core radius defined by our clumpfind method are used for showing the line width-radius relation of the identified cores. Since the different authors use the different definitions of the line width and core radius (Heyer & Brunt 2004; Caselli & Myers 1995; Larson 1981), we here convert the other line width-radius relations using our definitions.

Heyer & Brunt (2004) applied the PCA analysis to derive the relationship between the line width and the size inside the molecular clouds. Their line width Δv_{HB} and size L_{HB} correspond to the autocorrelation widths on both the spatial and the velocity axes. In the following, we transfer them into our FWHM line width and radius to do a direct comparison with our result.

If both a line and intensity profiles of a core can be approximated by Gaussian profiles, then the line width and size defined by Heyer & Brunt (2004) are given by $\Delta v_{\text{HB}} = 2\sigma_v$ and $L_{\text{HB}} = 2\sigma_L$, where σ_v and σ_L are the dispersions of the line and intensity profiles, respectively (see Heyer & Brunt 2004). On the other hand, the FWHM line width is defined as $\Delta v_{\text{FWHM}} = \sqrt{8 \ln 2} \sigma_v$. Thus, the FWHM line width can be rewritten as $\Delta v_{\text{FWHM}} = 1.18 \Delta v_{\text{HB}}$.

In the present paper, the core radius, R_{core} , is determined by taking the projected area enclosed by the 2σ level contour and by computing the radius of the circle required to reproduce the area. For a core with a Gaussian profile, our core radius is given by $R_{\text{core}} = L_{\text{HB}} \sqrt{\ln(T_{\text{peak}}/T_{\text{th}})}$, where T_{peak} and T_{th} are the peak antenna temperature and the threshold temperature of the 2σ level, respectively. From Table 1, the mean peak antenna temperature of the 68 identified cores is estimated to be $\langle T_{\text{peak}} \rangle = 1.14\text{K}$. If we adopt $\langle T_{\text{peak}} \rangle$ as a representative value, $R_{\text{core}} = 0.91 L_{\text{HB}}$.

According to Heyer & Brunt (2004), the linewidth-size relation for GMCs can be fitted by the power-law of $(\Delta v_{\text{HB}}/\text{km s}^{-1}) = 0.87(L_{\text{HB}}/\text{pc})^{0.65}$. Using $\Delta v_{\text{FWHM}} = 1.18 \Delta v_{\text{HB}}$ and $R_{\text{core}} = 0.91 L_{\text{HB}}$, the Heyer & Brunt relation can be rewritten as $(\Delta v_{\text{FWHM}}/\text{km s}^{-1}) = 1.09(R_{\text{core}}/\text{pc})^{0.65}$, which is shown by the dashed line in Figure 13a.

Caselli & Myers (1995) also used the different definition for the core radius. They used the half-maximum contour to define the core size. Assuming that a core has a Gaussian shape, the half-maximum radius is equal to $R_{\text{CM}} = \sqrt{\ln 2 / \ln(T_{\text{peak}}/T_{\text{th}})} R_{\text{core}}$, and $R_{\text{CM}} = 0.65 R_{\text{core}}$ for the mean peak antenna temperature of $\langle T_{\text{peak}} \rangle = 1.14\text{K}$. We thus replace the original Caselli & Myers relation, $(dv_{\text{NT}}/\text{km s}^{-1}) = 1.51(R_{\text{CM}}/\text{pc})^{0.53}$, with $(dv_{\text{NT}}/\text{km s}^{-1}) = 1.2(R_{\text{core}}/\text{pc})^{0.53}$.

Larson (1981) used the 3D velocity dispersion ($\sigma_{3\text{D}}$) and the maximum core size (L_{max}). Assuming that $L_{\text{max}} = 2R_{\text{core}}$, his original relation, $(\sigma_{3\text{D}}/\text{km s}^{-1}) = 1.1(L_{\text{max}}/\text{pc})^{0.38}$, is rewritten as $(\Delta v_{\text{FWHM}}/\text{km s}^{-1}) = 1.9(R_{\text{core}}/\text{pc})^{0.38}$.

This work is supported in part by a Grant-in-Aid for Scientific Research of Japan (19204020, 20540228) and a Grant for Promotion of Niigata University Research Projects. We thank Jes Jørgensen for kindly giving us the data of YSOs in L1688. We also thank Zhi-Yun Li, Doug Johnstone, and Philippe André for valuable comments, and Chris Brunt and Mark Heyer for helpful comments that improved the presentation of §5.4 and the Appendix.

REFERENCES

Abergel, A. et al. 1996, A&A, 315, L329

- Aikawa, Y., Herbst, E., Roberts, H., & Caselli, P. 1995, *ApJ*, 620, 330
- Allen, L. et al. 2006. in *Protostars and Planets V*, eds. B. Reipurth, D. Jewitt, and K. Keil (The University of Arizona Press), p. 361
- André, P., Ward-Thompson, D. & Barsony, M. 1993, *ApJ*, 406, 122
- André, P., Ward-Thompson, D. & Barsony, M. 2000, in *Protostars and Planets IV*, p. 59
- André, P., Belloche, A., Motte, F., & Peretto, N. 2007, *A&A*, 472, 519
- Ballesteros-Paredes, J., Klessen, R., Vázquez-Semadeni, E. 2003, *ApJ*, 592, 188
- Ballesteros-Paredes, J. & Mac Low, M.-M. 2002, *ApJ*, 570, 748
- Bate, M. R., Bonnell, I. A., & Bromm, V. 2003, *MNRAS*, 339, 577
- Benson, P.J. & Myers, P.C. 1989, *ApJS*, 71, 89
- Bertoldi, F. & McKee, C. F. 1992, *ApJ*, 395, 140
- Bonnell, I. A., Clark, P., Bate, M., & Pringle, J. E. 2001, *MNRAS*, 368, 573
- Bonnell, I. A., Clark, P., & Bate, M. 2008, *MNRAS*, 389, 1556
- Bontemps, S. et al. 2001, *A&A*, 372, 173
- Brunt, C. M. 2003, *ApJ*, 583, 280
- Butner, H. M., Lada, E. A., & Loren, R. B. 1995, *ApJ*, 448, 207
- Carpenter, J. M. 2000, *AJ*, 120, 3139
- Caselli, P. & Myers, P. C. 1995, *ApJ*, 446, 665
- Crutcher, R. M., Troland, T. M., Goodman, A. A., Heiles, C. Kazes, I., & Myers, P. C. 1993, *ApJ*, 407, 175
- Crutcher, R. M., 1999, *ApJ*, 520, 706
- Dame, T. M., Elmegreen, B. G., Cohen, R. S., & Thaddeus, P. 1986, *ApJ*, 305, 892
- Dib, S., Kim, J., Vázquez-Semadeni, E., Burkert, A., & Ahadmehri, M. 2007, *ApJ*, 61, 262
- Di Francesco, J., André, P., & Myers, P. C. 2004, *ApJ*, 617, 425
- Dobashi, K. et al. 2001, *PASJ*, 53, 85
- Elmegreen, B. G. 1979, *ApJ*, 232, 729

- Elmegreen, B. G. 2000, MNRAS, 530, 277
- Enoch, M. L., Evans, N. J. II, Sargent, A. I., Glenn, J., Rosolowsky, E., Myers, P. C. 2008, ApJ, 684, 1240
- Frerking, M. A., Langer, W. D., & Wilson, R. W. 1982, ApJ, 262, 590
- Fuller, G. A. & Myers, P. C. 1992, ApJ, 384, 523
- Gammie, C. F., Lin, Y.-T., Stone, J. M., & Ostriker, E. C. 2003, ApJ, 592, 203
- Genzel, R., Reid, M. J., Moran, M. J., & Downes, D. 1981, ApJ, 262, 590
- Gomez, G. C. Vázquez-Semadeni, E., Shadmehri, M., & Ballesteros-Paredes, J. 2007, ApJ, 669, 1042
- Heitsch, F., Hartmann, L. W. Burkert, A. 2008, ApJ, 683, 786
- Heyer, M. H. & Brunt, C. M. 2004, ApJ, 615, L45
- Heyer, M. H. & Brunt, C. M. 2007, in Triggered Star Formation in a Turbulent ISM, eds. B. G. Elmegreen & J. Palous, Cambridge University Press, pp. 9
- Henning, T., Michel, B., Stognienko, R. 1995, Planet. Space Sci., 43, 1333
- Hennebelle, P., Whitworth, A. P., Gladwin, P. P., & André, P. 2003, MNRAS, 340, 870
- Jijina, J., Myers, P. C., & Adams, F. C. 1999, ApJS, 125, 161
- Johnstone, D., Wilson, C. D., Moriarty-Schieven, G., Joncas, G., Smith, G., Gregersen, E., & Fich, M. 2000, ApJ, 545, 327
- Johnstone, D., Wilson, C. D., Moriarty-Schieven, G., Giannakopoulou-Creighton, J., & Gregersen, E. 2000, ApJS, 131, 505
- Johnstone, D., Di Francesco, J., & Kirk, H. 2004, ApJ, 611, 45
- Jørgensen, J. K., Johnstone, D., Kirk, H., Myers, P. C., Allen, L. E., & Shirley, Y. L. 2008, ApJ, 683, 822
- Krumholz, M. R., Mazner, C. D., & McKee, C. F. 2006, ApJ, 653, 361
- Krumholz, M. R. & Tan, J. C., 2007, ApJ, 656, 959
- Hartmann, L. 2001, AJ, 121, 1030
- Ikeda, N., Sunada, K., & Kitamura, Y. 2007, ApJ, 665, 1194
- Ikeda, N., Kitamura, Y., & Sunada, K. 2009, ApJ, 691, 1560

- Ikeda, N., & Kitamura, Y. 2009, ApJ, 705, L95
- Kamazaki, T., Saito, M., Hirano, N., Umemoto, T. & Kawabe, R. ApJ, 2003, 584, 357
- Klessen, R., Burkert, A., & Bate, M. R. 1998, ApJ, 501, L205
- Klessen, R., Heitsch, F., & Mac Low, M.-M. 2000, ApJ, 535, 887
- Knee, L. B. G. & Sandell, G. 2000, A&A, 361, 671
- Lada, E. A., DePoy, D.L., Evans, J. H. & Gatley, I. 1991, ApJ, 371, 171
- Lada, C.J. & Lada, E. A. 2003, ARA&A, 41, 57
- Li, Z.-Y. & Nakamura, F. ApJ, 2006, 640, L187
- Larson, R. B, 1981, MNRAS, 194, 809
- Loinard, L., Torres, R. M., Mioduszewski, A. J. & Rodriguez, L. F. 2008, ApJ, 675, L29
- Lombardi, M., Lada, C. J. & Alves, J. 2008, A&A, 480, 785
- Loren, R. T., & Wootten, A. 1986, ApJ, 306, 142
- Loren, R. T. 1989, ApJ, 338, 902
- Loren, R. T., Wootten, A. & Wilking, B. A. 1990, ApJ, 365, 269
- Mac Low, M.-M. 1999, ApJ, 524, 169
- Matzner, C. D. 2007, ApJ, 659, 1394
- McKee, C. F. & Ostriker, E. C. 2007, ARA&A, 45, 565
- Motte, F., André, P., & Neri, R. 1998, A&A, 336, 150
- Motte, F., André, P., Ward-Thompson, D. & Bontemps, S. 2001, A&A, 372, L41
- Myers, P. C. 1983, ApJ, 270, 105
- Myers, P. C., Ladd, E. F., & Fuller, G. A. 1991, ApJ, 372, L95
- Nakamura, F. & Li, Z.-Y. ApJ, 2007, 662, 395
- Nakamura, F. & Li, Z.-Y. ApJ, 2008, 687, 354
- Nakano, T. 1998, ApJ, 494, 587
- Nakano, T., Nishi, R. & Umebayashi, T. 2002, ApJ, 573, 199
- Nishi, R., Nakano, T., & Umebayashi, T. 1991, ApJ, 368, 181

- Norman, C., & Silk, J. 1980, ApJ, 238, 158
- Nutter, D., Kirk, J. M., Stamatellos, D. & Ward-Thompson, D. 2008, MNRAS, 384, 755
- Offner, S. S. R., Klein, R. I., & McKee, C. F. 2008, ApJ, 686, 1174
- Ossenkopf, V. & Mac Low, M.-M. 2002, A&A, 390, 307
- Ossenkopf, V. & Henning, T. 1994, A&A, 291, 943
- Ostriker, E. C., Stone, J. M., & Gammie, C. F., 2001, ApJ, 546, 980
- Padgett, D. L. et al. 2008, ApJ, 672, 1013
- Padoan, P. & Nordlund, A. 2002, ApJ, 576, 870
- Pineda, J., Rosolowsky, E. W., & Goodman, A. A. 2009, ApJ, 699, L134
- Plume, R., Jaffe, D. T., & Evans II, N. J. 1997, ApJ, 476, 730
- Poulton, C. J., Robitaille, T. P., Greaves, J. S., Bonnell, I. A., Williams, J. P., & heyer, M. H. 2008, MNRAS, 384, 1249
- Quillen, A. C., Thorndike, S. L., Cunningham, A., Frank, A., Gutermuth, R. A., Blackman, E. G., Pipher, J. L., & Ridge, N. 2005, ApJ, 632, 941
- Reid, M. A. & Wilson, C. D. 2006, ApJ, 644, 990
- Román-Zúniga, C. G., Elston, R., Ferreira, B., & Lada, E. A. 2008, ApJ, 672, 861
- Rosolowsky, E. 2005, PASP, 117, 1403
- Saito, H., Saito, M., Yonekura, Y., & Nakamura, F. 2008, ApJS, 178, 302
- Sandell, G. & Knee, L. B. G. 2000, ApJ, 546, L49
- Solomon, P. M., Rivolo, A. R., Barrett, J., & Yahil, A. 1987, ApJ, 319,
- Sanders, D. B., Scoville, N. Z., & Solomon, P. M. 1985, ApJ, 289, 373
- Schneider, N. & Brooks, K. 2004, PASA, 21, 290
- Simpson, R. J., Nutter, D., & Ward-Thompson, D. 2008, MNRAS, 391, 205
- Smith, R. J., Clark, P. C., & Bonnell, I. A. 2008, MNRAS, 391, 1091
- Stamatellos, D., Whitworth, A. P., & Ward-Thompson, D. 2007, MNRAS, 379, 1390
- Stanke, T., Smith, M. D., Gredel, R. & Khanzadyan, T. 2006, A&A, 447, 609

- Stone, J. M., Ostriker, E. C., & Gammie, C. F. 1998, *ApJ*, 508, L99
- Swift, J. J., Wilch, W. J. 2008, *ApJS*, 174, 202
- Tachihara, K. Mizuno, A., Fukui, Y. 2000, *ApJ*, 528, 817
- Tachihara, K. Onishi, T., Mizuno, A., Fukui, Y. 2002, *A&A*, 385, 909
- Testi, L. & Sargent, A. I. 1998, *ApJ*, 508, L91
- Tilley, D. & Pudritz, R. 2004, *MNRAS*, 353, 769
- Troland, T. H., Crutcher, R. M., Goodman, A. A., Heiles, C., Kazés, I., & Myers, P. C., 1996, *ApJ*, 471, 302
- Van Dishoeck, E. F., Blake, G. A., Jansen, D. J. & Groesberck, T. D. 1995, *ApJ*, 447, 760
- Vázquez-Semadeni, E., Kim, J., Shadmehri, M., & Ballesteros-Paredes, J., *ApJ*, 618, 344
- Volgenau, N. H., Mundy, L. G., Looney, L. W., & Welch, W. J. 2006, *ApJ*, 651, 301
- Walsh, A. J., Myers, P. C., Di Francesco, J., Mohanty, S., Bourke, T. L., Gutermuth, R. & Wilner, D. 2007, *ApJ*, 655, 958
- Wang, P., Li, Z.-Y., Abel, T., & Nakamura, F. 2009, *ApJ*, in press
- Williams, J. P., de Geus, E. J., & Blitz, L. 1994, *ApJ*, 428, 693
- Wilking, B. A., Gagné, M., Allen, L. E. 2009, in *Handbook of Star Forming Regions Vol. II* in press
- Wilson, K. E. et al. 1999, *ApJ*, 513, L139
- Whitworth, A., Bate, M. R., Nordlund, A., Reipurth, B. & Zinnecker, H. 2007, in *Protstars and Planets V*, eds. B. Reipurth, D. Jewitt, and K. Keil, (University of Arizona Press), p.459

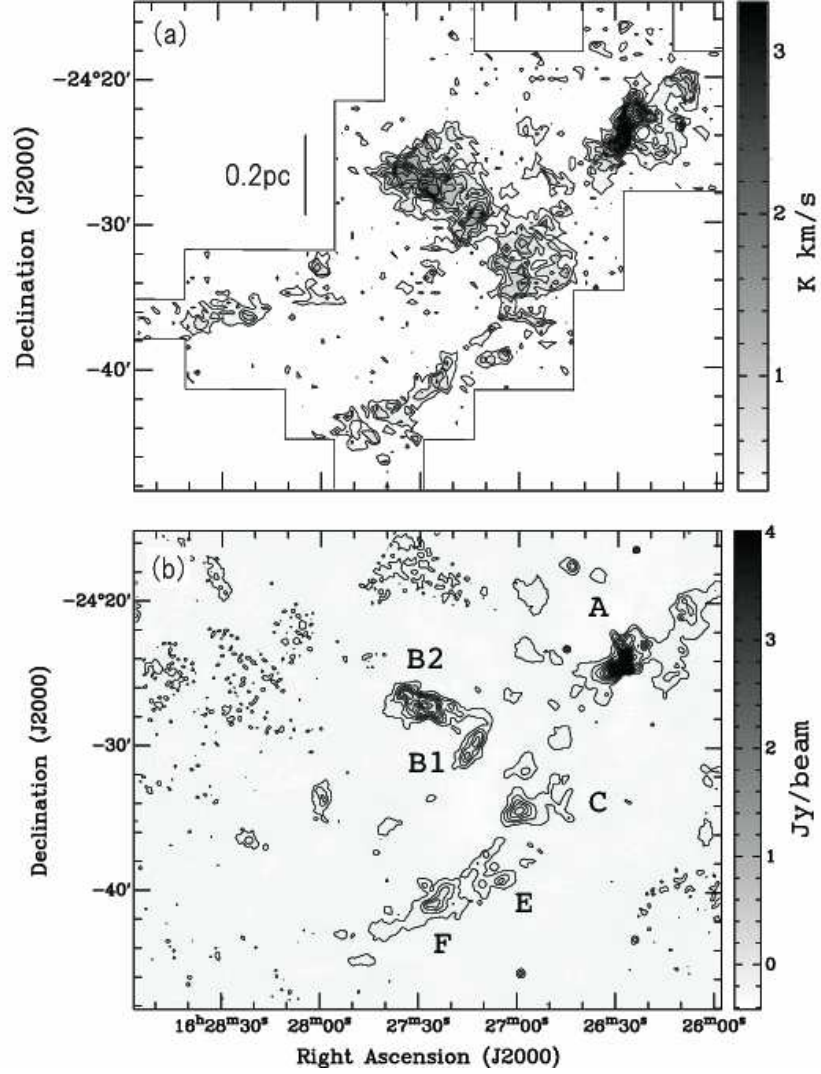


Fig. 1.— (a): H^{13}CO^+ ($J = 1-0$) total integrated intensity map in the velocity range of $v_{\text{LSR}} = 1-6$ km s^{-1} toward the ρ Ophiuchi main cloud. The grey scale indicates the integrated intensity in units of K km s^{-1} . The contours start from 0.3 K km s^{-1} , corresponding to the 3σ noise level, at intervals of 0.2 K km s^{-1} . (b): $850\mu\text{m}$ image of the same area as in panel (a), obtained with the SCUBA at the JCMT. The grey scale indicates the intensity in linear scale from -0.4 to 4 Jy beam^{-1} . The contours start from 0.2 Jy beam^{-1} at intervals of 0.2 Jy beam^{-1} . The dense subclumps are designated by A, B1, B2, C, E, and F.

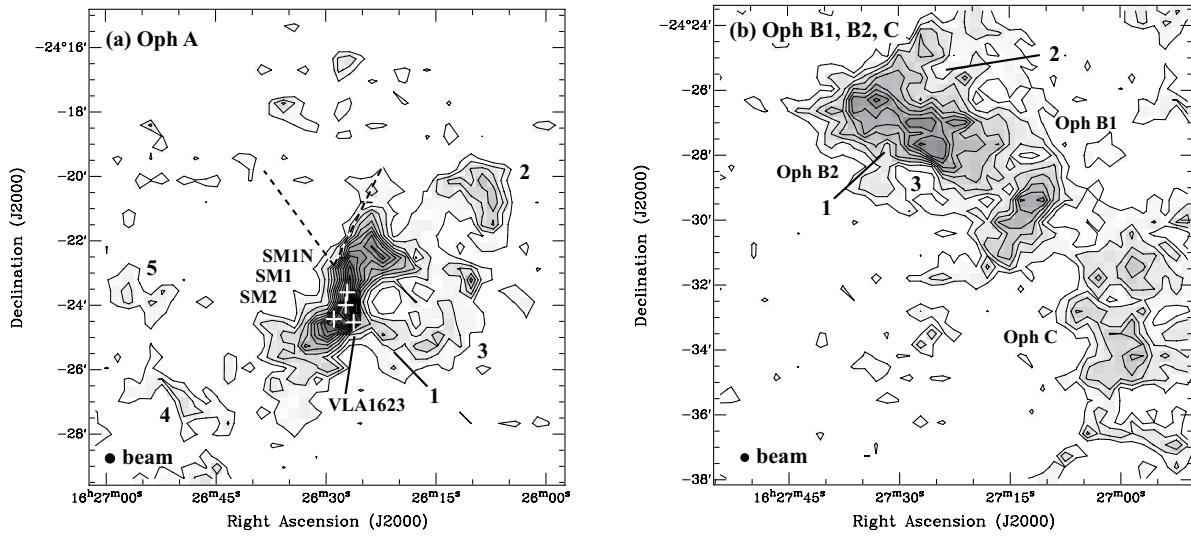


Fig. 2.— H^{13}CO^+ ($J = 1 - 0$) total integrated intensity maps taken with the Nobeyama 45 m telescope toward (a) the Oph A region and (b) the Oph B1, B2, and C regions. The grey scale and contours are the same as those of Figure 1a. In panel (a), the two dashed lines indicate the position of the filaments seen in the $850\mu\text{m}$ map (Wilson et al. 1999). The positions of the submillimeter sources, SM1, SM1N, and SM2, and the prototypical Class 0 object, VLA 1623, are indicated by crosses. In each panel the arcs and holes discussed in the text are indicated by numbers. The beam size of the Nobeyama 45 m telescope is shown at the lower left corner of each panel.

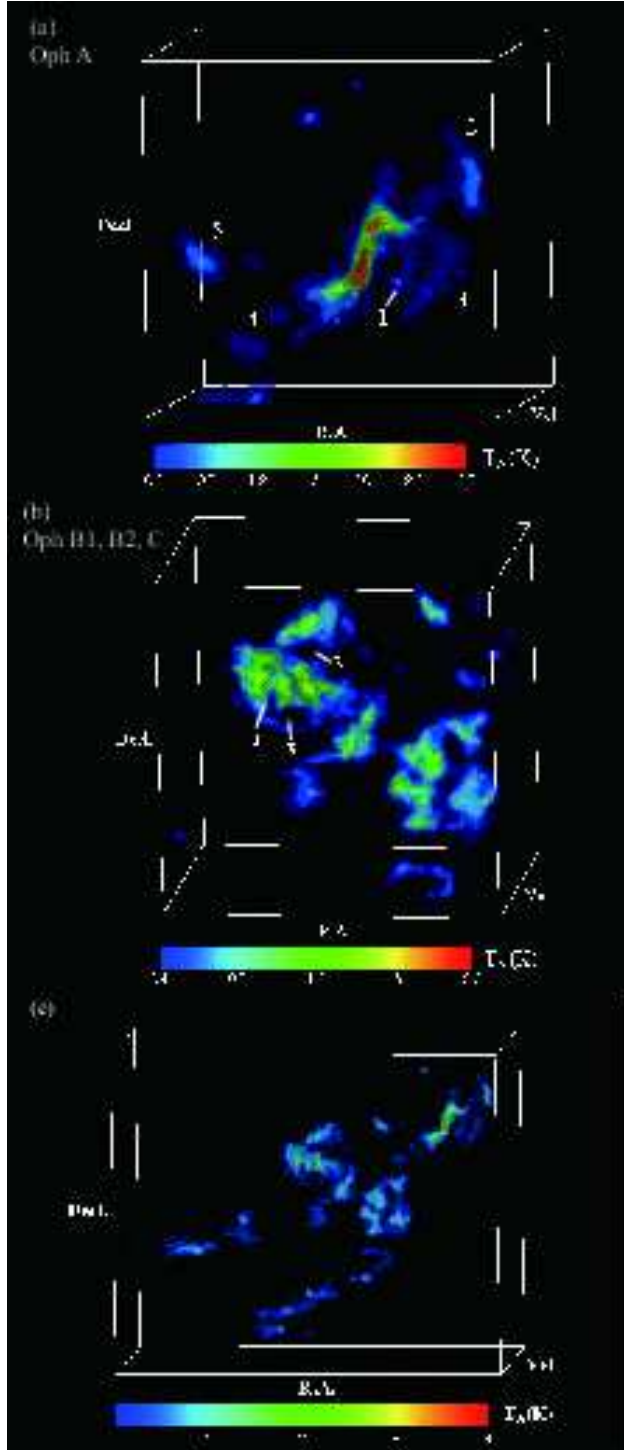


Fig. 3.— Three-dimensional representation of the antenna temperature (T_A^*) in the α - δ - v_{LSR} space toward (a) the Ophi A region, (b) the Ophi B1, B2, and C regions, and (c) the whole observed area. For panels (a) and (b), the areas projected on the plane of the sky are the same as those of Figures 2a and 2b, respectively. The color shows the iso-temperature surfaces. The color bar indicates the antenna temperature in units of K. In each panel the numbers have the same meaning as in Figure 2. (Mpeg animations of Figs. 2a, 2b, and 2c are available in the online journal.)

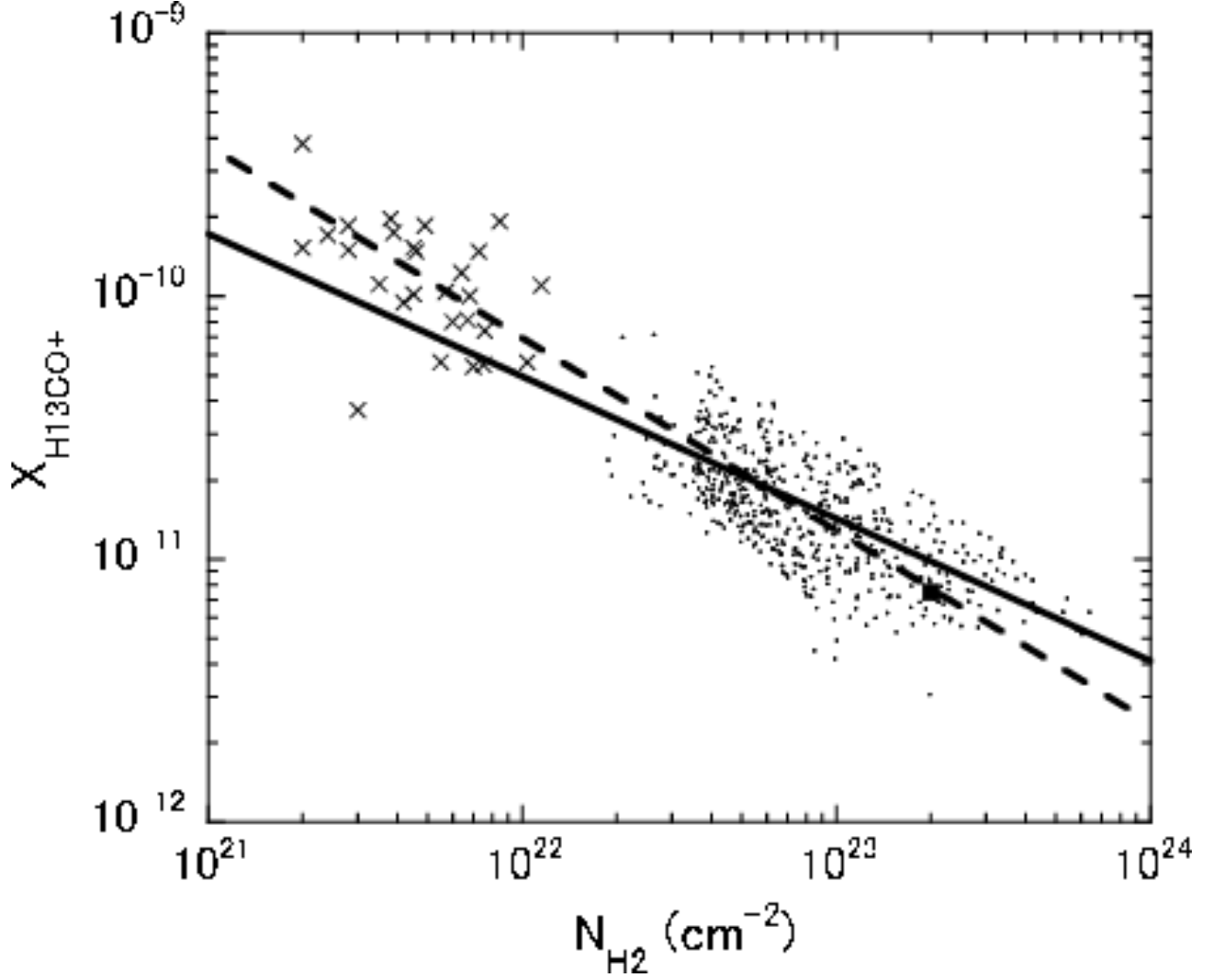


Fig. 4.— Fractional abundance of H^{13}CO^+ relative to H_2 against the H_2 column density in the ρ Ophiuchi main cloud. The solid line shows the best-fit power-law for the ρ Oph data. For comparison, the fractional abundances of H^{13}CO^+ derived by Butner et al. (1995) and van Dishoeck et al. (1995) are plotted by crosses and a filled square, respectively. The dashed line shows the best-fit power-law for both their data and ours.

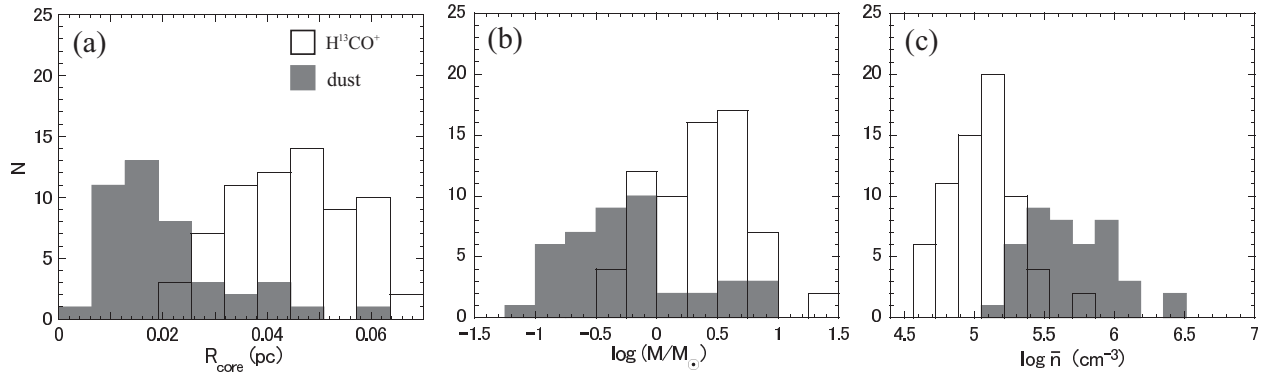


Fig. 5.— Histograms of (a) the radius, (b) core mass, (c) mean density of the H^{13}CO^+ cores (*open histograms*) and the $850 \mu\text{m}$ dust cores (*grey histograms*) in the ρ Ophiuchi main cloud.

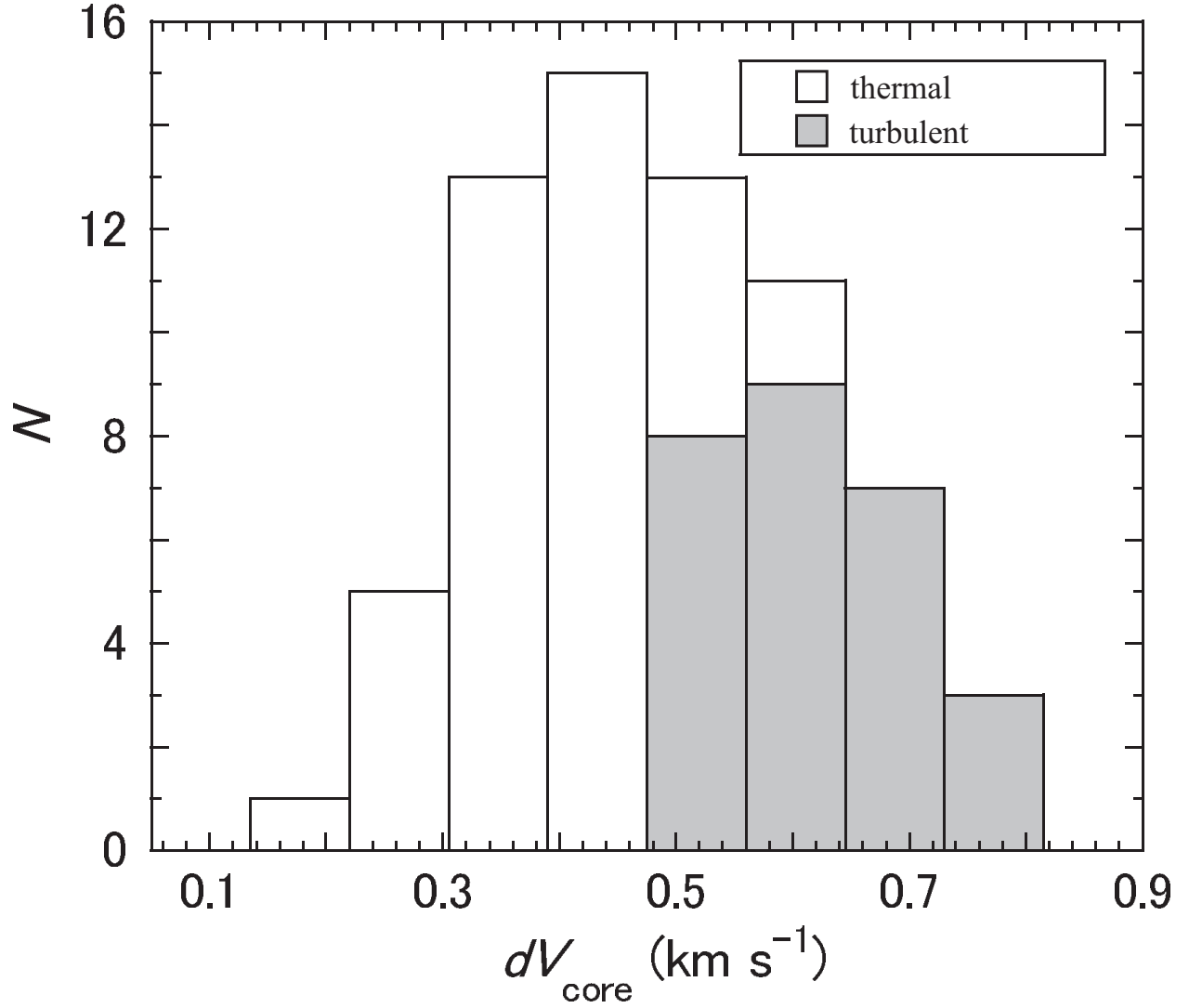


Fig. 6.— Histogram of the FWHM line width of the H^{13}CO^+ cores in the ρ Ophiuchi main cloud. The open and grey histograms indicate the thermal and turbulent cores, respectively. Note that the gas temperature is assumed to be 12 K for all the cores except for those located in the Oph A region, for which $T = 18$ K.

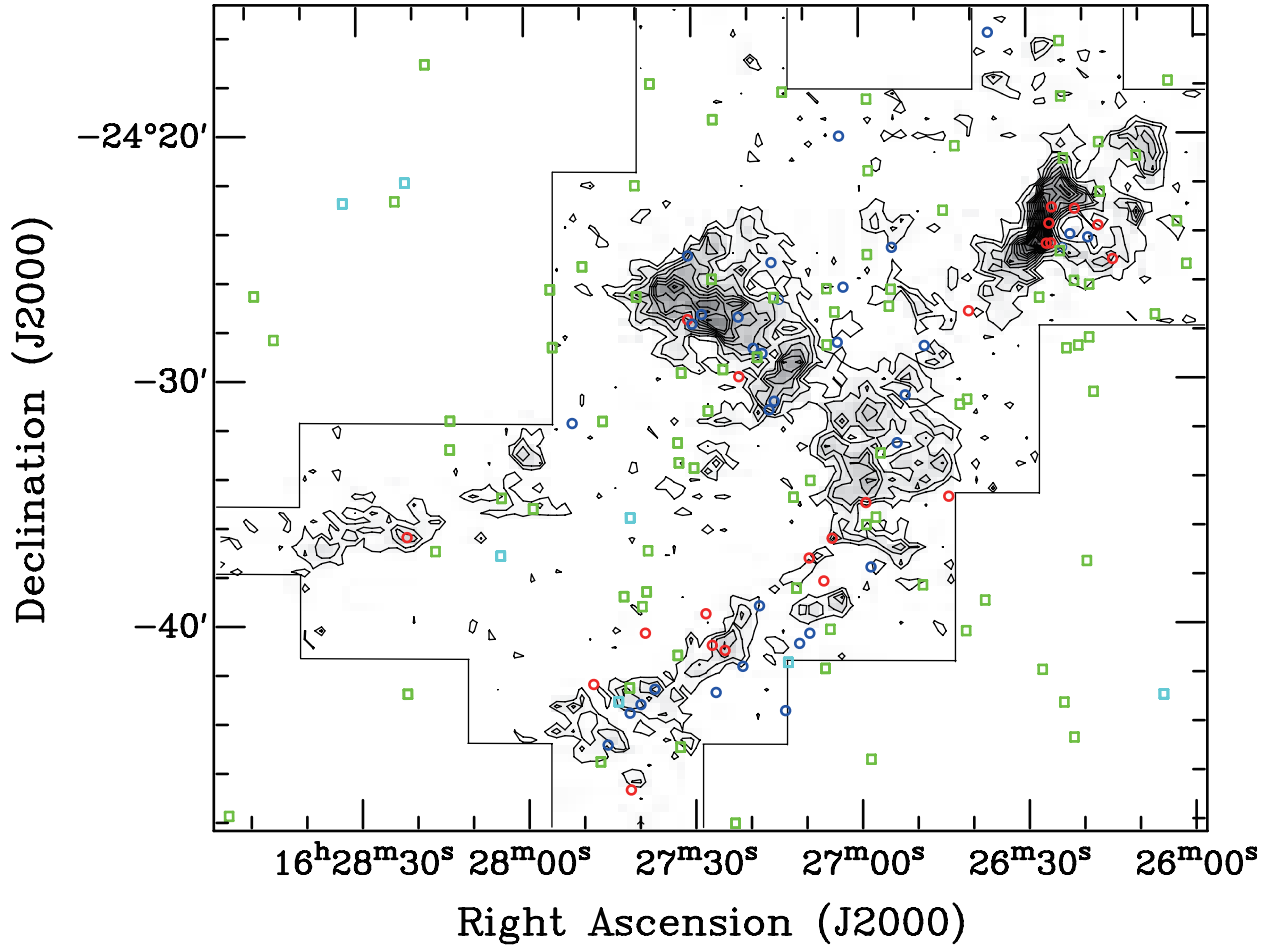


Fig. 7.— Distribution of YSOs identified with the Spitzer Space telescope. Contours indicate the total integrated intensity of the H^{13}CO^+ ($J = 1 - 0$) emission, as shown in Figure 1a. The red and blue circles are for Class I sources including Class 0 and Flat Spectrum sources, respectively. The green and cyan squares are for Class II and Class III sources, respectively. The cores associated with the circles are defined as protostellar cores in this study.

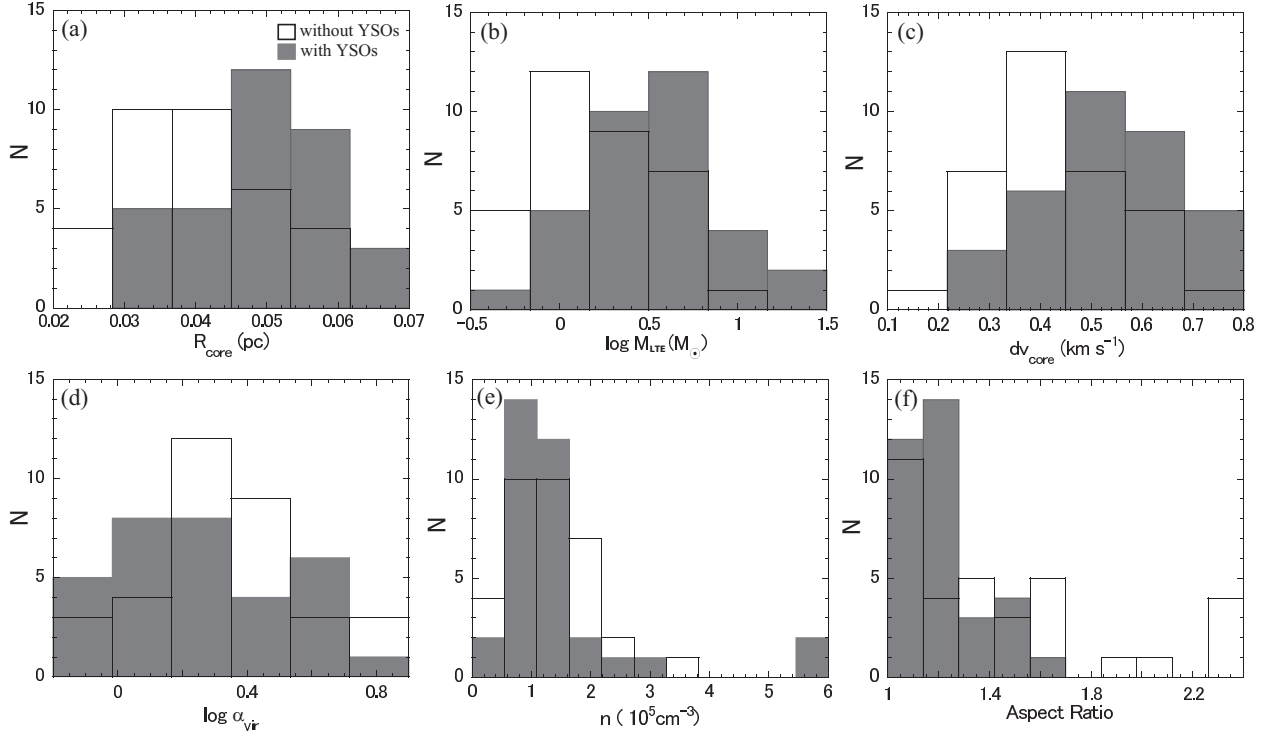


Fig. 8.— Histograms of (a) the radius, (b) LTE mass, (c) FWHM line width, (d) virial ratio, (e) mean density, and (f) aspect ratio of the H^{13}CO^+ cores. For each panel, the open and grey histograms are for the cores without and with YSOs, respectively.

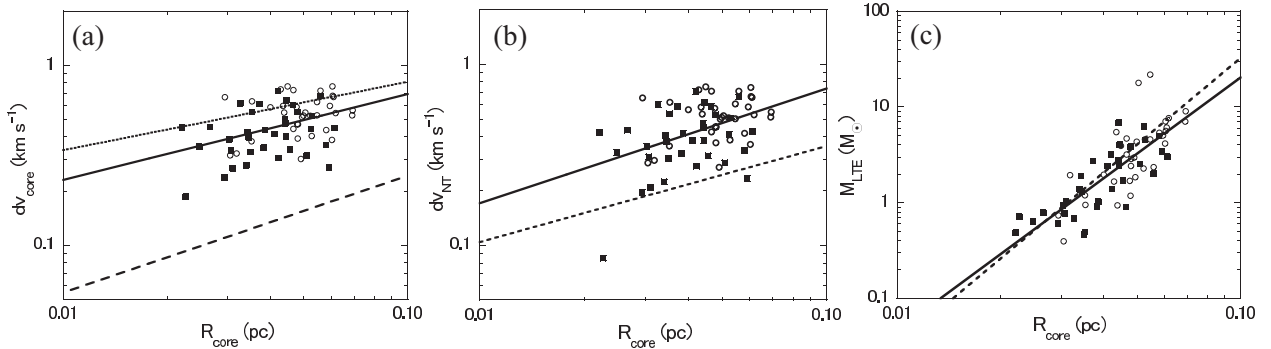


Fig. 9.— (a) Line width-radius relation, (b) Nonthermal line width-radius relation, and (c) Mass-radius relation of the H^{13}CO^+ cores. The filled squares and open circles are for the cores without and with YSOs, respectively. In each panel, the best-fit power-law is indicated by the solid line. In panel (a) the Larson and Heyer & Brunt relations are plotted by the dotted and dashed lines, respectively. Note that we extrapolated these relations down to 0.01 pc, for comparison. In panels (b) and (c), the dashed lines indicate the Caselli & Myers relation and the relation of $M_{\text{LTE}} = 4\pi\mu m_H \bar{n} R_{\text{core}}^3 / 3$ ($\propto R_{\text{core}}^3$), respectively.

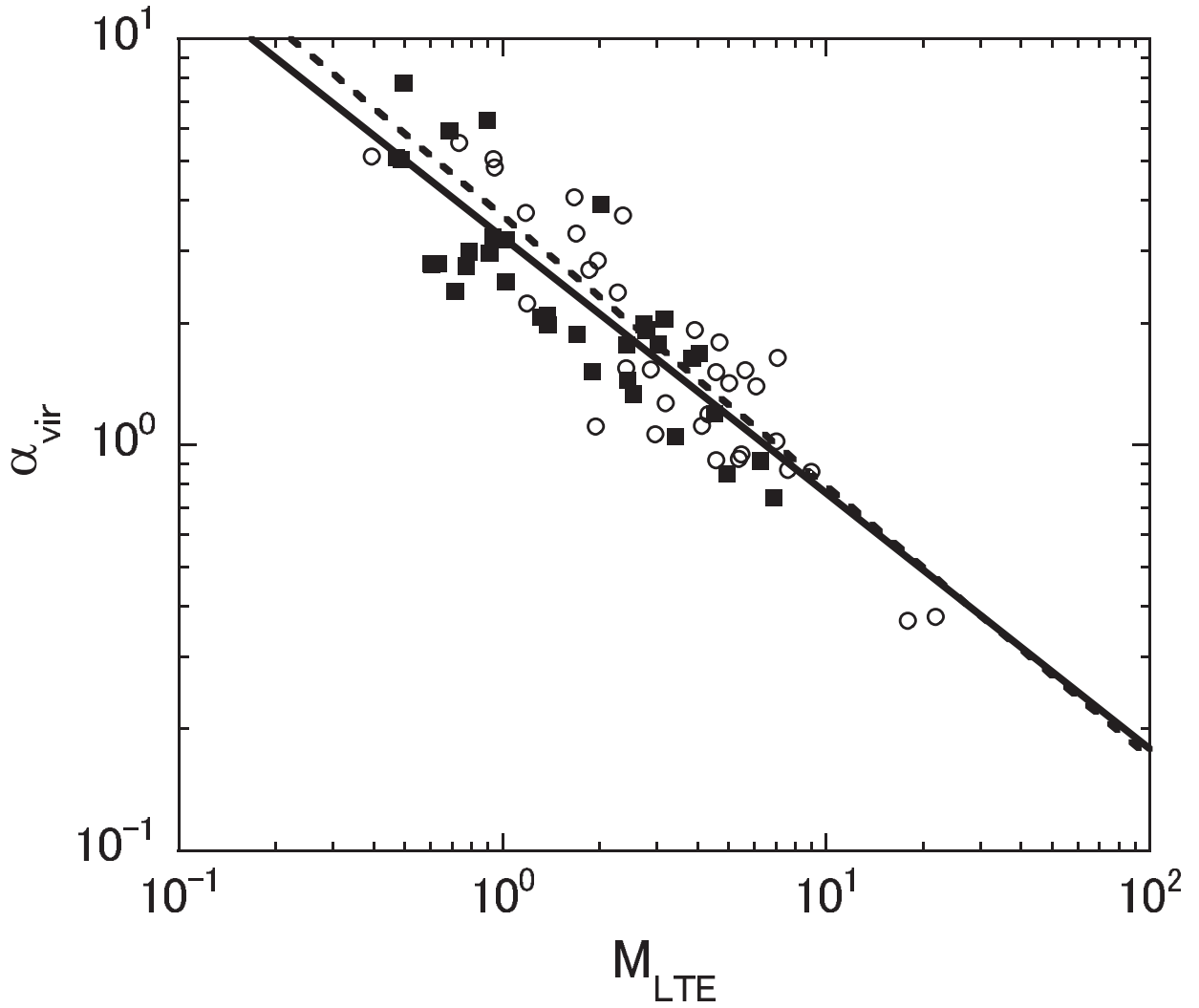


Fig. 10.— Virial ratio-mass relation of the H^{13}CO^+ cores. The filled squares and open circles are the same as those in Figure 9. The virial ratio of a self-gravitating core confined by ambient pressure is indicated by the dashed line (Bertoldi & McKee 1992).

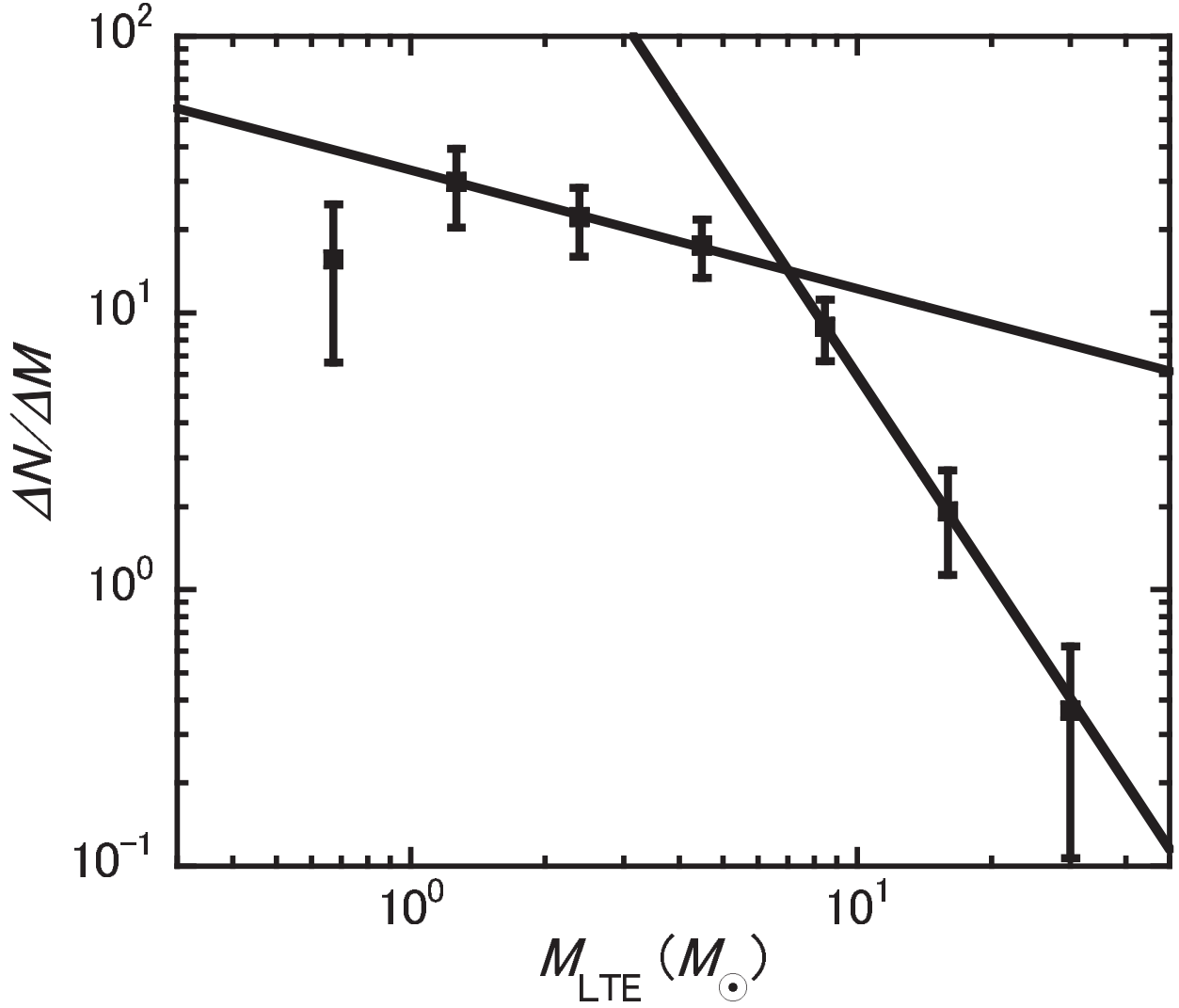


Fig. 11.— Mass spectrum of the H^{13}CO^+ cores in the ρ Ophiuchi main cloud. The error bars correspond to \sqrt{N} counting statistics, where N is the number of cores in each mass bin. The solid lines are the least square fits in the interval of $1M_{\odot} \lesssim M_{\text{LTE}} \lesssim 7M_{\odot}$ ($\Delta N/\Delta M \propto M_{\text{LTE}}^{-0.43}$) and $M_{\text{LTE}} \gtrsim 7M_{\odot}$ ($\Delta N/\Delta M \propto M_{\text{LTE}}^{-2.4}$).

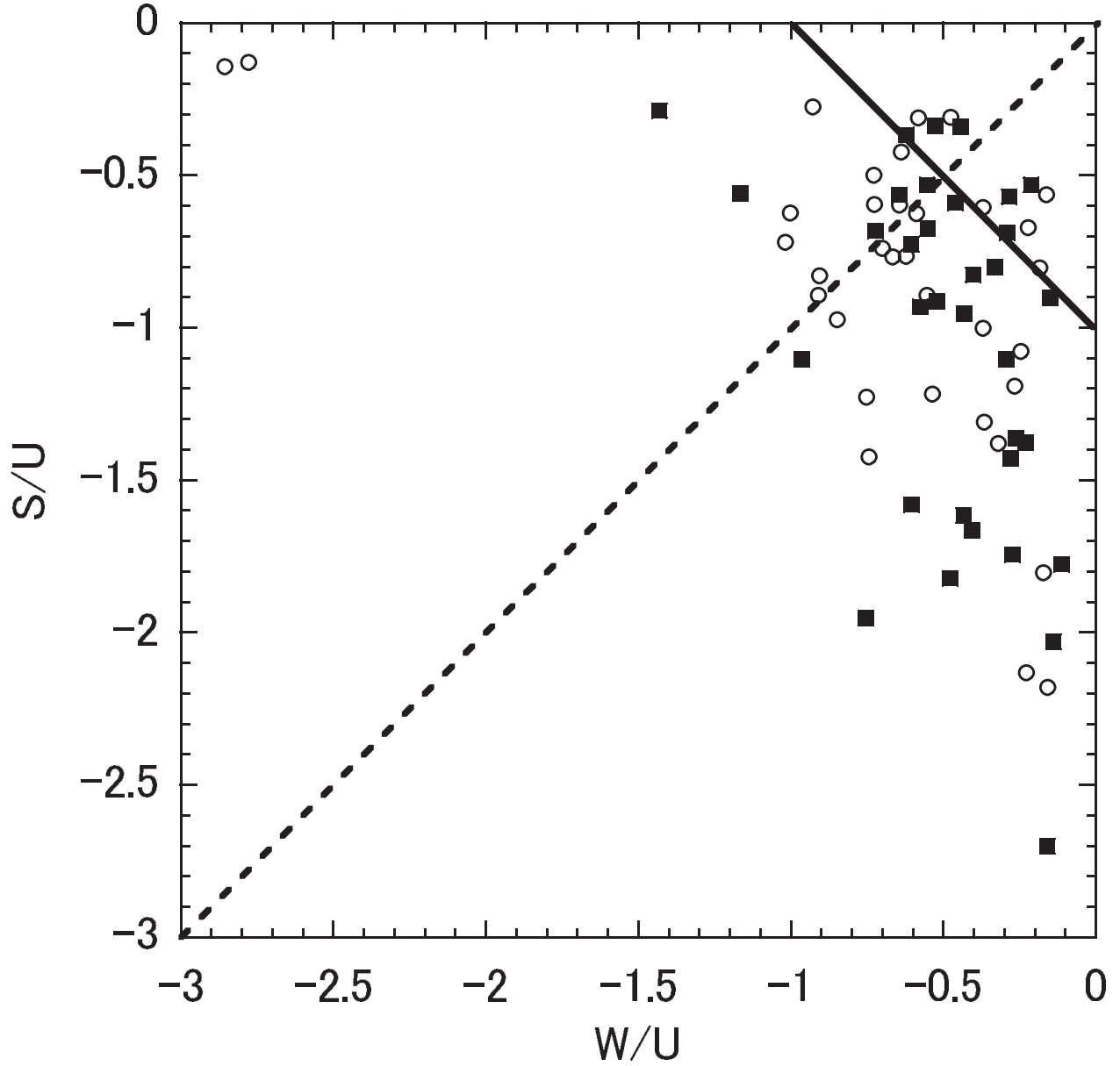


Fig. 12.— Relationship between the surface term, S , and the gravitational term, W , in the virial equation. They are normalized to the internal kinetic energy term, U [Note that $W/U = -(\alpha_{\text{vir}})^{-1}$]. The solid line indicates the virial equilibrium, $U + W + S = 0$. The dashed line indicates the line at which $W = S$. For the cores that lie below the solid line, the value of $U + W + S$ is negative and thus expected to be bound. All others are unbound and expected to disperse away, if they do not gain more mass through accretion and/or merging with other cores, or reduce internal support through turbulence dissipation. The filled squares and open circles are the same as those in Figure 9.

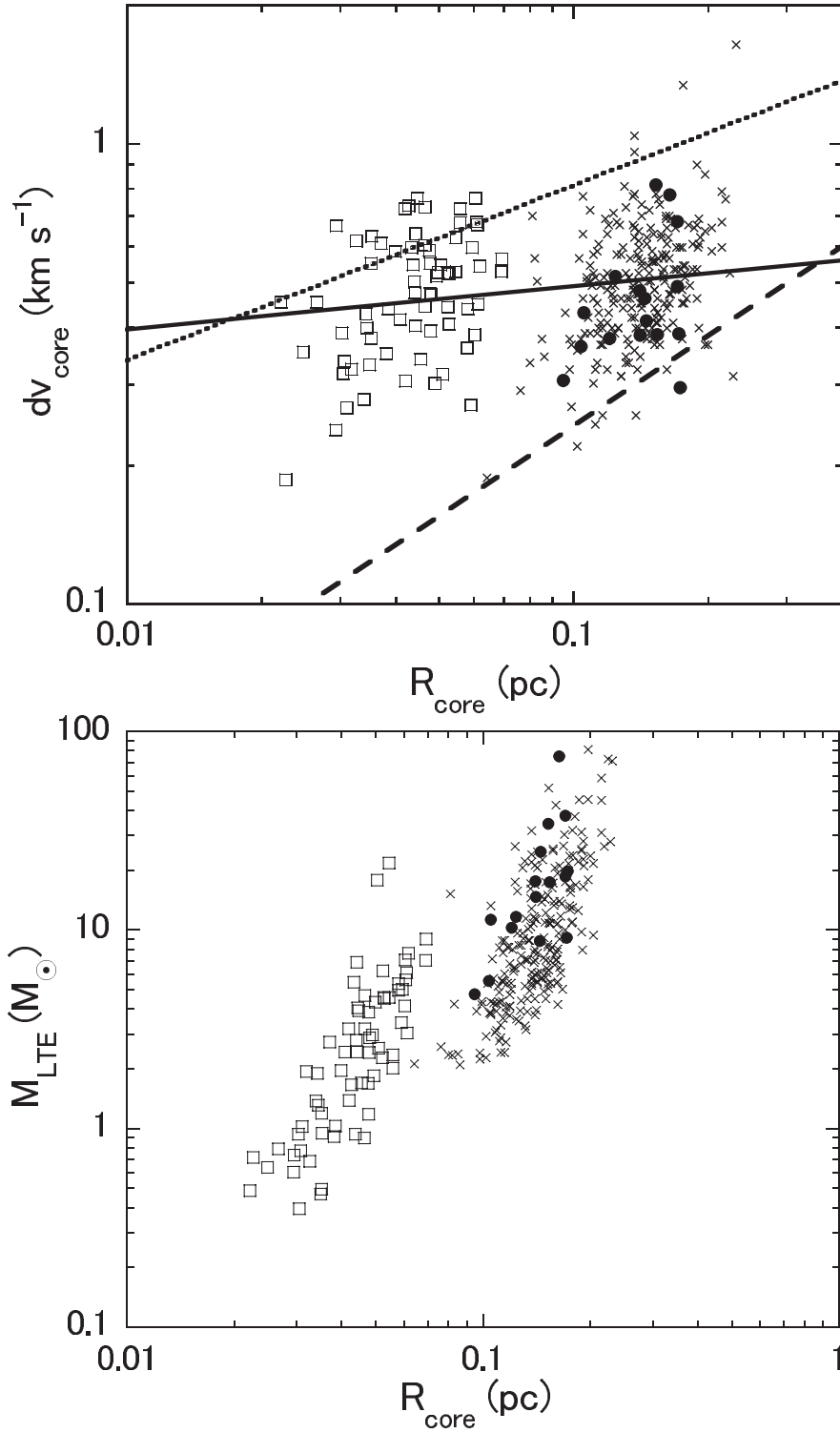


Fig. 13.— Line width-radius relation (*upper panel*) and mass-radius relation (*lower panel*) of the H^{13}CO^+ cores toward the ρ Ophiuchi main cloud (*open squares*) and toward the Orion A molecular cloud (*crosses*). The ρ Oph cores identified from the smoothed data are indicated by filled circles, for comparison. The solid line in the upper panel indicates the best-fit power-law for the ρ Oph cores identified from both the original and smoothed data. The dotted and dashed lines indicate the Larson and the Heyer & Brunt relations, respectively.

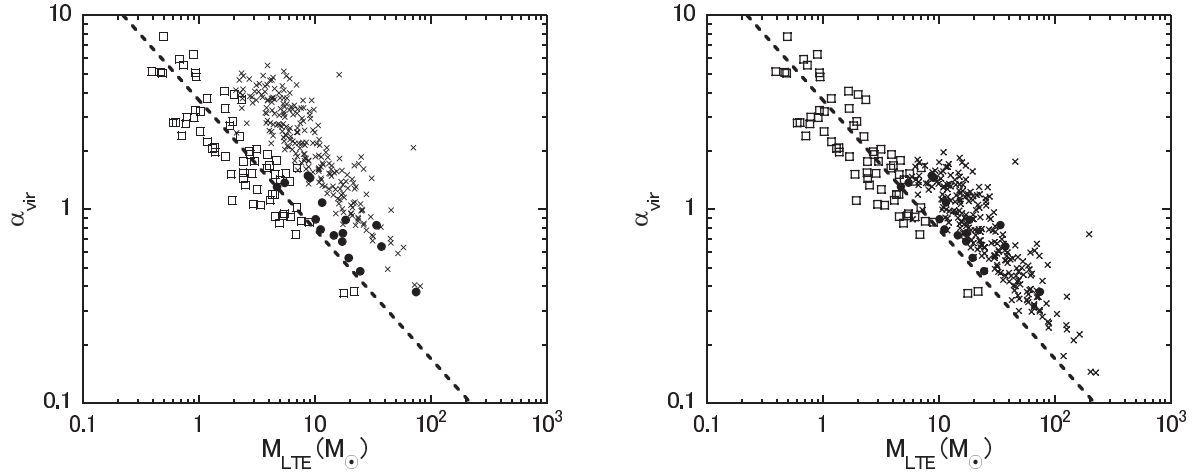


Fig. 14.— Virial ratio-mass relation of the ρ Oph cores and the Orion A cores. For Orion A, the fractional abundances of H^{13}CO^+ are set to 4.8×10^{-11} (adopted by Ikeda et al. 2007) and 1.72×10^{-11} (adopted for ρ Oph in the present paper) in panels (a) and (b), respectively. The open squares, crosses, and filled circles are the same as those of Figure 13. The dashed lines are the same as that of Fig. 10. Note that the Jeans mass given by eq. [2.13] of Bertoldi & McKee (1992) is almost the same for both the original and smoothed ρ Oph cores.

Table 1. Properties of the H^{13}CO^+ cores in the ρ Ophiuchi main cloud

ID	R.A. (J2000.0)	Decl. (J2000.0)	v_{LSR} (km s^{-1})	$T_{A,\text{peak}}^*$ (K)	R_{core} (arcsec)	R_{core} (pc)	Aspect Ratio	dv_{core} (km s^{-1})	M_{LTE} (M_{\odot})	M_{vir} (M_{\odot})	α_{vir}	\bar{n} (10^5 cm^{-3})	YSOs ^a
1	16 26 7.3	-24 20 27.6	3.15	1.50	72.9	0.0442	2.33	0.476	6.89	5.10	0.74	3.31	N
2	16 26 10.3	-24 23 12.0	3.41	0.87	99.7	0.0604	1.19	0.764	7.07	11.6	1.64	1.33	Y
3	16 26 13.3	-24 20 6.7	3.02	0.70	72.7	0.0441	1.67	0.502	2.78	5.32	1.91	1.34	N
4	16 26 14.8	-24 21 8.3	3.41	0.78	78.8	0.0478	1.05	0.551	3.85	6.28	1.63	1.47	N
5	16 26 19.4	-24 23 32.0	2.76	0.69	90.0	0.0545	1.52	0.528	4.57	6.89	1.51	1.17	Y
6	16 26 22.4	-24 24 54.0	3.28	1.05	76.8	0.0466	1.34	0.730	4.68	8.35	1.79	1.92	Y
7	16 26 23.8	-24 20 26.5	3.41	0.99	73.3	0.0444	1.07	0.639	4.06	6.82	1.68	1.92	N
8	16 26 26.7	-24 16 40.1	3.80	0.53	36.5	0.0221	1.42	0.453	0.49	2.46	5.03	1.86	N
9	16 26 26.9	-24 22 29.8	3.28	3.27	83.2	0.0504	1.34	0.547	17.88	6.59	0.37	5.77	Y
10	16 26 26.9	-24 23 52.0	3.80	3.99	90.0	0.0545	1.20	0.627	21.78	8.19	0.38	5.56	Y
11	16 26 28.4	-24 23 31.4	2.76	0.79	65.9	0.0399	1.62	0.585	1.97	5.58	2.83	1.28	Y
12	16 26 33.0	-24 24 12.2	3.02	0.99	67.6	0.0410	1.28	0.415	2.43	4.27	1.76	1.46	N
13	16 26 33.0	-24 26 15.6	3.15	1.12	61.3	0.0371	1.26	0.609	2.73	5.41	1.98	2.21	N
14	16 26 34.5	-24 25 55.0	3.54	1.39	86.3	0.0523	1.11	0.442	6.25	5.70	0.91	1.81	N
15	16 26 36.0	-24 25 34.3	3.15	0.69	51.2	0.0311	1.23	0.267	1.03	2.58	2.52	1.42	N
16	16 26 43.5	-24 25 54.3	3.80	0.78	56.1	0.0340	1.19	0.279	1.38	2.87	2.08	1.46	N
17	16 26 45.1	-24 26 56.0	3.93	0.83	37.4	0.0227	1.96	0.186	0.72	1.71	2.39	2.55	N
18	16 26 45.3	-24 33 26.8	3.80	1.17	113.8	0.0690	1.24	0.528	7.02	7.15	1.02	0.89	Y
19	16 26 46.5	-24 23 50.7	3.02	0.63	50.1	0.0304	2.28	0.388	0.93	3.02	3.24	1.38	N
20	16 26 46.6	-24 27 57.6	3.80	0.53	50.3	0.0305	1.27	0.316	0.39	2.02	5.13	0.58	Y
21	16 26 49.6	-24 26 55.7	3.93	0.85	43.9	0.0266	1.11	0.454	0.79	2.36	2.98	1.73	N
22	16 26 49.7	-24 30 0.8	3.80	1.23	99.4	0.0602	1.03	0.385	4.14	4.60	1.11	0.79	Y
23	16 26 52.9	-24 36 52.0	4.45	0.92	58.2	0.0353	1.37	0.550	0.49	3.83	7.76	0.47	N
24	16 26 52.9	-24 37 12.5	4.71	0.98	50.7	0.0307	2.10	0.337	0.77	2.13	2.76	1.10	N
25	16 26 55.9	-24 36 31.2	4.58	0.95	63.6	0.0386	1.37	0.438	1.03	3.30	3.20	0.75	N
26	16 26 57.0	-24 23 50.0	3.80	1.37	79.1	0.0480	1.02	0.393	2.41	3.72	1.54	0.91	Y
27	16 26 57.3	-24 31 22.6	3.93	1.52	101.9	0.0618	1.21	0.543	7.63	6.61	0.87	1.34	Y
28	16 26 57.4	-24 37 53.4	4.58	0.66	48.6	0.0295	1.06	0.666	0.74	4.07	5.54	1.19	Y
29	16 27 1.9	-24 34 47.9	3.67	1.56	100.5	0.0609	1.24	0.669	6.09	8.46	1.39	1.11	Y
30	16 27 3.4	-24 36 10.1	4.97	0.95	58.1	0.0352	1.28	0.379	1.19	2.66	2.23	1.13	Y

Table 1—Continued

ID	R.A. (J2000.0)	Decl. (J2000.0)	v_{LSR} (km s ⁻¹)	$T_{\text{A,peak}}^*$ (K)	R_{core} (arcsec)	R_{core} (pc)	Aspect Ratio	dv_{core} (km s ⁻¹)	M_{LTE} (M_{\odot})	M_{vir} (M_{\odot})	α_{vir}	\bar{n} (10 ⁵ cm ⁻³)	YSOs ^a
31	16 27 3.5	-24 38 54.7	4.58	1.29	56.5	0.0343	1.65	0.427	1.89	2.87	1.51	1.95	N
32	16 27 4.7	-24 26 54.7	3.67	0.47	72.2	0.0438	1.07	0.547	0.94	4.73	5.05	0.46	Y
33	16 27 6.3	-24 32 44.2	4.06	1.52	87.0	0.0528	1.14	0.523	4.53	5.41	1.20	1.28	N
34	16 27 9.6	-24 39 35.4	4.32	1.03	78.5	0.0476	1.11	0.587	1.69	5.59	3.31	0.65	Y
35	16 27 10.7	-24 27 35.4	4.32	0.71	81.4	0.0493	1.29	0.516	1.85	4.99	2.70	0.64	Y
36	16 27 10.8	-24 29 18.2	3.80	1.38	73.9	0.0448	1.19	0.765	3.92	7.51	1.92	1.81	Y
37	16 27 12.2	-24 25 52.4	3.41	0.77	78.8	0.0478	1.15	0.472	1.18	4.39	3.72	0.45	Y
38	16 27 12.3	-24 29 59.3	3.80	1.37	69.2	0.0420	1.49	0.722	3.17	6.48	2.04	1.78	N
39	16 27 14.0	-24 38 12.8	4.71	0.65	53.9	0.0327	2.27	0.616	0.69	4.07	5.94	0.81	N
40	16 27 15.3	-24 30 40.2	3.67	1.37	100.0	0.0606	1.21	0.678	5.61	8.58	1.53	1.05	Y
41	16 27 18.2	-24 27 55.5	3.41	0.78	92.1	0.0558	1.13	0.723	2.35	8.63	3.67	0.56	Y
42	16 27 21.1	-24 23 48.4	3.15	1.15	79.3	0.0481	1.08	0.471	2.87	4.41	1.54	1.07	Y
43	16 27 21.2	-24 26 53.6	4.45	1.26	98.0	0.0594	1.15	0.596	5.02	7.11	1.42	0.99	Y
44	16 27 21.6	-24 39 55.2	4.84	0.96	70.6	0.0428	1.11	0.735	1.66	6.78	4.07	0.88	Y
45	16 27 24.3	-24 27 55.1	3.80	1.76	82.2	0.0498	1.04	0.527	4.33	5.15	1.19	1.45	Y
46	16 27 24.7	-24 40 56.7	4.84	0.83	58.3	0.0353	1.26	0.631	0.95	4.55	4.81	0.89	Y
47	16 27 25.7	-24 24 29.3	3.02	1.70	95.7	0.0580	1.15	0.438	5.37	4.96	0.92	1.14	Y
48	16 27 25.8	-24 27 13.8	3.80	1.93	71.7	0.0435	1.12	0.595	5.47	5.19	0.95	2.76	Y
49	16 27 26.0	-24 33 24.1	3.54	0.97	100.9	0.0612	1.56	0.449	3.02	5.35	1.77	0.55	N
50	16 27 28.8	-24 27 34.2	4.45	1.87	86.9	0.0527	1.21	0.405	4.58	4.20	0.92	1.30	Y
51	16 27 29.2	-24 41 37.5	3.67	0.79	86.1	0.0522	1.13	0.525	2.27	5.37	2.37	0.66	Y
52	16 27 30.7	-24 40 35.7	4.32	1.38	84.0	0.0509	1.62	0.316	2.53	3.37	1.33	0.79	N
53	16 27 33.3	-24 26 11.6	3.93	1.63	114.2	0.0692	1.46	0.563	8.99	7.72	0.86	1.12	Y
54	16 27 33.3	-24 26 52.7	4.58	1.97	95.6	0.0579	1.01	0.361	4.96	4.21	0.85	1.06	N
55	16 27 33.3	-24 28 35.6	3.80	0.76	92.1	0.0558	1.12	0.675	2.01	7.85	3.90	0.48	N
56	16 27 36.5	-24 34 4.5	3.41	0.51	76.6	0.0465	2.33	0.603	0.90	5.64	6.29	0.37	N
57	16 27 38.3	-24 41 16.4	3.54	0.53	57.7	0.0350	1.61	0.331	0.47	2.39	5.10	0.45	N
58	16 27 42.9	-24 42 38.3	3.80	1.06	76.8	0.0466	1.51	0.444	3.19	4.03	1.26	1.31	Y
59	16 27 46.0	-24 44 41.6	3.67	1.31	80.8	0.0490	1.53	0.302	2.97	3.16	1.06	1.05	Y
60	16 27 51.9	-24 42 58.3	3.93	1.02	75.1	0.0455	1.02	0.341	1.70	3.17	1.87	0.75	N

Table 1—Continued

ID	R.A. (J2000.0)	Decl. (J2000.0)	v_{LSR} (km s^{-1})	$T_{\text{A,peak}}^*$ (K)	R_{core} (arcsec)	R_{core} (pc)	Aspect Ratio	dv_{core} (km s^{-1})	M_{LTE} (M_{\odot})	M_{vir} (M_{\odot})	α_{vir}	\bar{n} (10^5 cm^{-3})	YSOs ^a
61	16 27 57.7	-24 35 4.8	4.19	0.97	56.9	0.0345	1.44	0.398	1.31	2.71	2.06	1.32	N
62	16 27 59.2	-24 34 23.6	4.19	0.75	41.0	0.0248	1.01	0.353	0.64	1.78	2.80	1.72	N
63	16 28 0.6	-24 33 1.2	4.32	1.34	73.0	0.0442	1.05	0.402	2.43	3.51	1.44	1.16	N
64	16 28 3.7	-24 34 43.8	4.19	0.75	48.5	0.0294	1.68	0.238	0.60	1.68	2.79	0.99	N
65	16 28 6.7	-24 34 23.1	4.32	0.71	62.9	0.0381	1.14	0.350	0.91	2.71	2.97	0.68	N
66	16 28 15.8	-24 35 44.7	4.19	1.06	69.5	0.0421	1.04	0.306	1.38	2.74	1.98	0.77	N
67	16 28 20.4	-24 36 25.6	4.19	1.60	52.6	0.0319	1.11	0.324	1.94	2.15	1.11	2.48	Y
68	16 28 26.4	-24 36 4.6	4.19	1.20	97.4	0.0590	1.34	0.271	3.42	3.58	1.05	0.69	N

Note. — Units of right ascension are hours, minutes, and seconds, and units of declination are degrees, arcminutes, and arcseconds. Cores No. 1 through 17 and 19 are located in the Oph A region and the temperature is set to be 18K. For the other cores, $T = 12\text{K}$. The typical uncertainties of R_{core} and dv_{core} are, respectively, about 0.01 pc, derived from the uncertainty in the estimation of the core projected area, and the velocity resolution of 0.13 km s^{-1} .

^aY and N mean, respectively, the cores associated with and without YSOs that are classified as either Class I or Flat Spectrum objects based on the Spitzer observations.

Table 2. Summary of the Physical Properties of the H^{13}CO^+ cores

Property	Minimum	Maximum	Mean ^a	Median
R_{core} (pc)	0.0221	0.0692	0.0450 ± 0.0113	0.0451
dv_{core} (km s^{-1})	0.186	0.765	0.488 ± 0.142	0.474
M_{LTE} (M_{\odot})	0.39	21.79	3.35 ± 3.57	2.42
$M_{\text{vir}}/M_{\text{LTE}}$	0.368	7.76	2.37 ± 1.57	1.89
\bar{n} (cm^{-3})	3.70×10^4	5.77×10^5	$(1.35 \pm 0.96) \times 10^5$	1.35×10^5
Aspect Ratio	1.01	2.33	1.34 ± 0.33	1.22

^aWith standard deviation

Table 3. Summary of the Physical Properties of the $850\mu\text{m}$ cores

Property	Minimum	Maximum	Mean ^a	Median
R_{core} (pc)	0.00494	0.0601	0.0204 ± 0.0118	0.0174
M_{LTE} (M_{\odot})	0.0868	8.25	1.42 ± 2.13	0.553
\bar{n} (cm^{-3})	1.41×10^5	3.20×10^6	$(6.53 \pm 6.29) \times 10^5$	4.37×10^5

^aWith standard deviation

Note. — The uniform temperature of $T = 15$ K is assumed for all the cores in Jørgensen et al. (2008).

Table 4. Summary of the Physical Properties of the H¹³CO⁺ cores with and without YSOs

Property	Minimum	Maximum	Mean ^a	Median
Cores without YSOs				
R_{core} (pc)	0.0221	0.0612	0.0403 ± 0.0105	0.0398
dv_{core} (km s ⁻¹)	0.186	0.722	0.431 ± 0.132	0.421
M_{LTE} (M _⊙)	0.469	6.89	1.54 ± 1.69	1.54
$M_{\text{vir}}/M_{\text{LTE}}$	0.74	7.76	2.63 ± 1.65	2.05
\bar{n} (cm ⁻³)	3.70×10^4	3.31×10^5	$(1.29 \pm 0.66) \times 10^5$	1.30×10^5
Aspect Ratio	1.01	2.33	1.45 ± 0.417	1.36
Cores with YSOs				
R_{core} (pc)	0.0295	0.0692	0.0497 ± 0.0102	0.0492
dv_{core} (km s ⁻¹)	0.302	0.765	0.544 ± 0.130	0.545
M_{LTE} (M _⊙)	0.394	21.8	4.55 ± 4.48	3.55
$M_{\text{vir}}/M_{\text{LTE}}$	0.37	5.54	2.11 ± 1.46	1.53
\bar{n} (cm ⁻³)	0.449×10^5	5.77×10^5	$(1.40 \pm 1.20) \times 10^5$	1.12×10^5
Aspect Ratio	1.02	1.62	1.22 ± 0.155	1.19

^aWith standard deviation